SPATIAL PATTERNS OF SEDIMENT TRANSPORT

IN THE UPPER WILLAMETTE RIVER, OREGON

by

TREVOR BROOKS LANGSTON

A THESIS

Presented to the Department of Geography
and the Graduate School of the University of Oregon
in partial fulfillment of the requirements
for the degree of
Master of Science

June 2015

THESIS APPROVAL PAGE

Student: Trevor Brooks Langston

Title: Spatial Patterns of Sediment Transport in the Upper Willamette River, Oregon

This thesis has been accepted and approved in partial fulfillment of the requirements for the Master of Science degree in the Department of Geography by:

Mark Fonstad	Chairperson
Patricia McDowell	Member

and

Scott L. Pratt	Dean of the Graduate School

Original approval signatures are on file with the University of Oregon Graduate School.

Degree awarded June 2015

THESIS ABSTRACT

Trevor Brooks Langston

Master of Science

Department of Geography

June 2015

Title: Spatial Patterns of Sediment Transport in the Upper Willamette River, Oregon

The Willamette is a gravel-bed river that drains ~28,800 square kilometers between the Coast Range and Cascade Range in northwestern Oregon before entering the Columbia River near Portland. In the last 150 years, natural and anthropogenic drivers have altered the sediment transport regime, drastically reducing the geomorphic complexity of the river. The purpose of this research is to assess longitudinal trends in sediment transport within the modern flow regime. Sediment transport rates are highly discrete in space, exhibit similar longitudinal patters across flows and increase non-linearly with flow. The highest sediment transport rates are found where the channel is confined due to disconnection of the floodplain and the river runs against high resistance terraces. The spatial distributions of sediment transport rates and active gravel are tightly linked. Sediment sampling revealed slight downstream fining in the surface grain size. Sediment size did not correlate with stream power.

CURRICULUM VITAE

NAME OF AUTHOR: Trevor Brooks Langston

GRADUATE AND UNDERGRADUATE SCHOOLS ATTENDED:

University of Oregon, Eugene
University of Mary Washington, Fredericksburg, Virginia
University of North Carolina at Wilmington, Wilmington

DEGREES AWARDED:

Master of Science, Geography, June 2015, University of Oregon
Bachelor of Science, Geology, June 2009, University of Mary Washington

AREAS OF SPECIAL INTEREST:

Fluvial Geomorphology
Remote Sensing
Stream Restoration

PROFESSIONAL EXPERIENCE:

Graduate Teaching Fellow, University of Oregon, Eugene, Oregon, October 2013 – June 2015

Research Associate, United States Geological Survey, Reston, Virginia, March 2013 – September 2013, November 2009 – November 2011

Voluntary Teacher, Kataloni Secondary School, Machakos, Kenya, November 2011 – March 2013

ACKNOWLEDGMENTS

Foremost I wish to express sincere gratitude to my advisor Mark Fonstad for his mentorship and patience. Mark worked diligently to instill me with the tools and perspective of a critical scientist. I also wish to thank Patricia McDowell for her keen insight and critical questions that grounded my research along the way. Rose Wallick and the rest of the geomorphic team at the USGS Portland office contributed much to this project. Rose was always available for questions and has gone out of her way to foster my academic and professional development. Jojo Mangano and Heather Bervid helped me in the field on several hot summer days for which I am very appreciative. I wish to thank the Department of Geography for their support as a community and moneys awarded for summer research and conference presentations. Finally I would like to thank my family for caring for me all these years and encouraging me to pursue a graduate degree.

TABLE OF CONTENTS

Chapter Page

LIST OF FIGURES

Figure Page

LIST OF TABLES

CHAPTER I

INTRODUCTION

Determining the timing and rate of sediment transport is a fundamental problem in fluvial geomorphology. In the Willamette River, OR, there is a great need to understand how flow and sediment processes shape the fluvial landscape (Wallick et al., 2013). In the last 150 years, both natural and anthropogenic drivers have altered the sediment transport regime, drastically reducing the geomorphic complexity of the river (Benner & Sedell, 1997; S Gregory, Ashkenas, Oetter, Minear, & Wildman, 2002; Wallick, Grant, Lancaster, Bolte, & Denlinger, 2007). Previous dynamic multi-threaded river reaches have transformed into stable single channels to the detriment of aquatic habitats and ecosystem productivity (Stanley Gregory, 2007). Transplanted in time, Euro-Americans first settling along the Willamette in the 19th century may find the same river unrecognizable today. Consider the following account from 1875:

> Captain Miller, one of the oldest and most experienced pilots in shoal waters of the same nature as the Willamette, has stated that he has never run the same channel for two consecutive years between Harrisburg and Eugene ("Annual Reports of Chief of Engineers for the year 1875, Part II," 1875).

Today, the river more or less runs the same course year to year. Channel modifications in the 19th century have largely tempered historically dynamic processes the river was in constant readjustment to. Key drivers of basin-scale change have been snag removal, flow regulation by dams, revetments, gravel mining, and conversion of riparian forests to agriculture. Large, systematic morphological changes have occurred since Euro-American settlement including marked loss of gravel bars, secondary

channels and floodplain forests. The Willamette is predominantly an alluvial river, meaning that channel morphology is a direct consequence of sediment transport processes (Church, 2006; Lane & Richards, 1997). Fully alluvial reaches of the river have been most affected by basin controls on sediment and flow (Wallick et al., 2013). Understanding the transport processes that continue to drive morphological change is key for deconstructing the Willamette's past as well as for predicting its future.

Modification of the fluvial regime of the Willamette can largely be reduced to impacts on the timing and manner in which water and sediment move through the system. The transport of sediment is a first-order process in fluvial geomorphic systems, and therefore has the potential to affect the entire hierarchy of river parameters (Grant, 2012). There is much we don't know about the sediment regime of the Willamette River. Currently our knowledge of sediment dynamics along the mainstem Willamette is highly discrete or exists at the basin scale (Klingeman, 1987; O'Connor et al., 2014; Wallick et al., 2013). Describing the continuous spatial and temporal trends of sediment transport is necessary to build a process-based understanding of how the Willamette adjusts to drivers of the sediment transport regime.

Some of the most pressing questions for the Willamette today concern how sediment is transported by the river. What is the balance between the supply and demand of sediment? Where can we expect the river to aggrade or degrade? Answers to these questions comprise a holy grail for our understanding of process on the Willamette River (and are accordingly hard to answer). Recently, the importance of fluvial geomorphic knowledge has become increasingly self-evident as we learn more about the tight linkages between geomorphology, ecology and human systems (Baker et al., 2004; S.

Rice, Stoffel, Turowski, & Wolf, 2012). Sediment aggradation heightens the risk of flooding while sediment degradation can disconnect key off-channel habitats for in-stream fauna. Extinction and declining stocks of native salmon species in the Pacific Northwest are linked to loss of floodplain habitat (S. V. Gregory & Bisson, 1997). In the Willamette, the distribution of sediment is thought to be a limiting factor for the passage and spawning behavior of salmon (D. W. Hulse, Branscomb, Enright, Gregory, & Wildman, 2007). Degradation of the channel bed in the Willamette has led to disconnection from secondary features.

The transport of alluvium is a fundamental process in fluvial geomorphology with real, significant consequences for river systems and all intersecting spheres: human, ecological or otherwise. Yet little is known today about how the Willamette moves sediment. This study attempts to provide a building block in our understanding of the sediment regime of the Willamette River by characterizing modern sediment transport processes. Specifically, we aim to answer the following question:

What are the key characteristics of the modern sediment transport regime, and what is the longitudinal pattern of these characteristics in the Upper Willamette River, Oregon?

The Upper Willamette River was historically the most dynamic section of the river. This remains true today though it has suffered the greatest loss in geomorphic complexity of any section along the Willamette. There is a large potential to increase aquatic habitat because many previously active features are still imprinted on the floodplain. Previous and ongoing restoration in the Upper Willamette has sought to

reconnect relict features for ecosystem benefit. The line of investigation we undertake in this study will inform both restoration activities and further scientific research. The largest component of our work is to analyze sediment transport in relation to distance downstream and flow magnitude.

CHAPTER II

BACKGROUND

Physical Characterization

The Willamette River Basin (Fig. 1) is a subduction forearc basin covering around 30,000 km^2 in northwestern Oregon lying between the Cascade Range to the west and Coast Range to the east (D. Hulse, Gregory, & Baker, 2002). A diverse assemblage of events during the Quaternary has resulted in a complex stratigraphic record. These events include regional uplift, deglaciation and catastrophic glacial outburst floods from Lake Missoula (O'Connor, Sarna-Wojcick, Woznikak, Polette, & Fleck, 2001). The valley floor in which the mainstem lies is an extensive alluvial plain (typically between 20 and 50 km in width) occasionally punctuated by hills of moderate relief. The valley floor is bounded by large alluvial fans where it abuts the degrading mountain ranges to the east and west. The basin has a Mediterranean climate with cool wet winters and warm dry summers. Up to 80% of annual precipitation falls between October and March with only 5% falling between July and August. Precipitation increases sharply with elevation from 100 – 130 cm annually in the valley bottom to 500 cm near the watershed boundaries in the Coast and Cascade ranges (D. Hulse et al., 2002).

The Willamette River is a gravel-bed alluvial river that flows northwards for 300 km from its source at the confluence at the Coast Fork and Middle Fork Rivers near Eugene, Oregon to its confluence with the Columbia in Portland, Oregon. In the U.S. it is the 13th largest river by discharge. Major tributaries along its length include the McKenzie, Santiam and Clackamas rivers. Willamette Falls, a large natural waterfall near Oregon City, controls the base level of the river upstream.

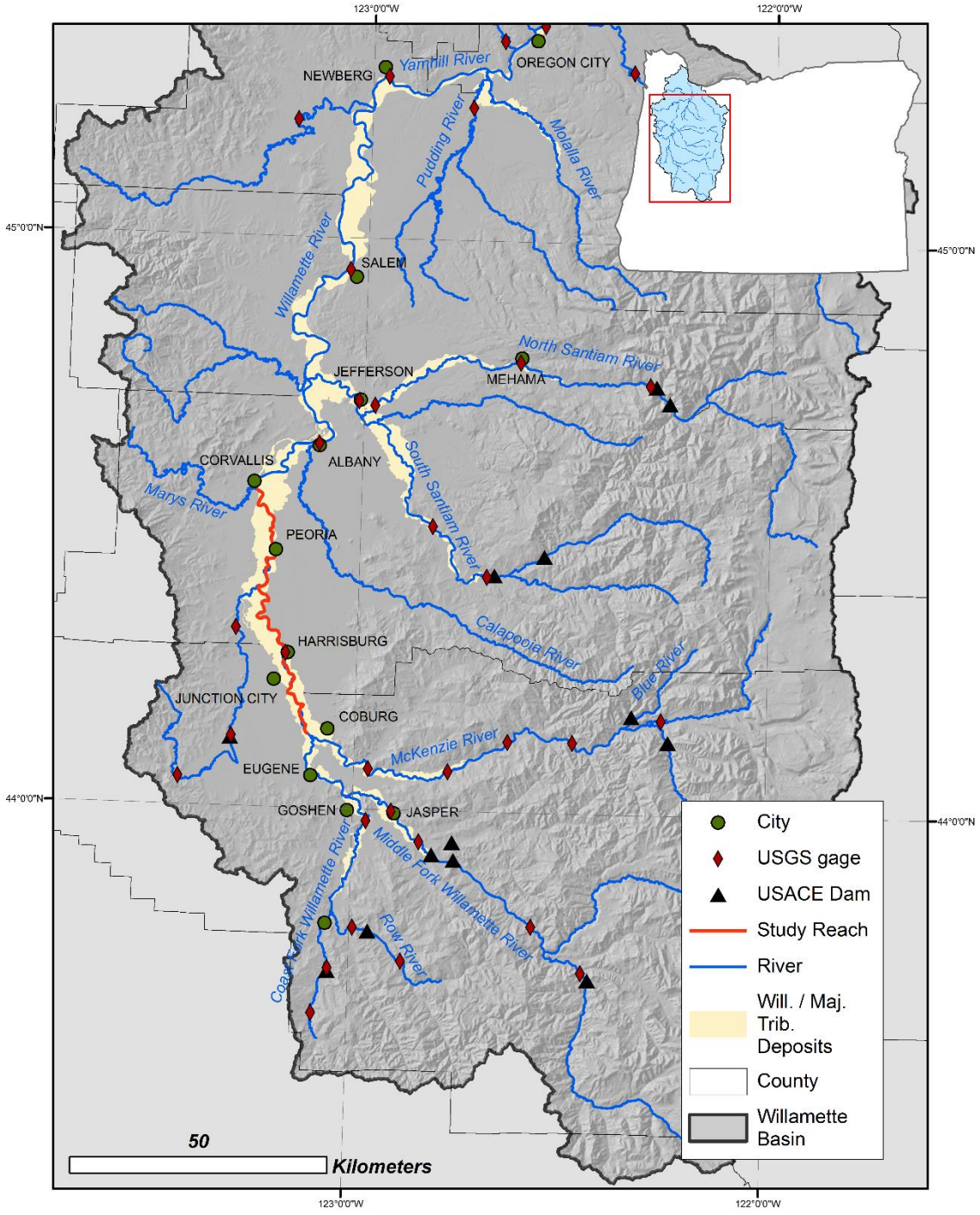

Figure 1. Basin map of the Willamette Valley, Oregon. The study segment is highlighted in red.

The mainstem is typically classified into three geomorphically distinct segments. Moving downstream from its head at the confluence of the Coast Fork and Middle Fork Willamette Rivers these are: the Upper segment upstream of Corvallis, the Middle segment upstream of Willamette Falls and the Lower segment stretching from the falls to the confluence with the Columbia. The focus area of this study is a 67 kilometer segment of the Upper Willamette that spans from the McKenzie confluence near Coburg, Oregon to Corvallis, Oregon.

The Upper Willamette (Fig. 2) is the steepest and most dynamic segment along the mainstem. A report on Quaternary units in the Willamette Valley by O'Connor (2001) identified three separate geologic units within this section. Broad gravel braidplains deposited in the Pleistocene between 15 and 12.7 ka (Qg2) underlie slack-water deposits of the Missoula Floods (Qff2). The Willamette floodplain during the Holocene (Qalc) incised into Qff2 to expose Qg2 material where the river meanders against pre-Holocene terraces.

Holocene alluvium (Qalc) is unconsolidated, highly permeable and a substantial conduit for groundwater entering the Willamette. Sand and gravel deposits dominate strata between base flow elevation and 3 meters above. Fine sand, silt and clay make up higher overbank deposits. Pleistocene deposits (Qg2) are formed of sand and gravel, are weakly-cemented and develop locally into resistant ledges when exposed by the river (O'Connor et al., 2001).

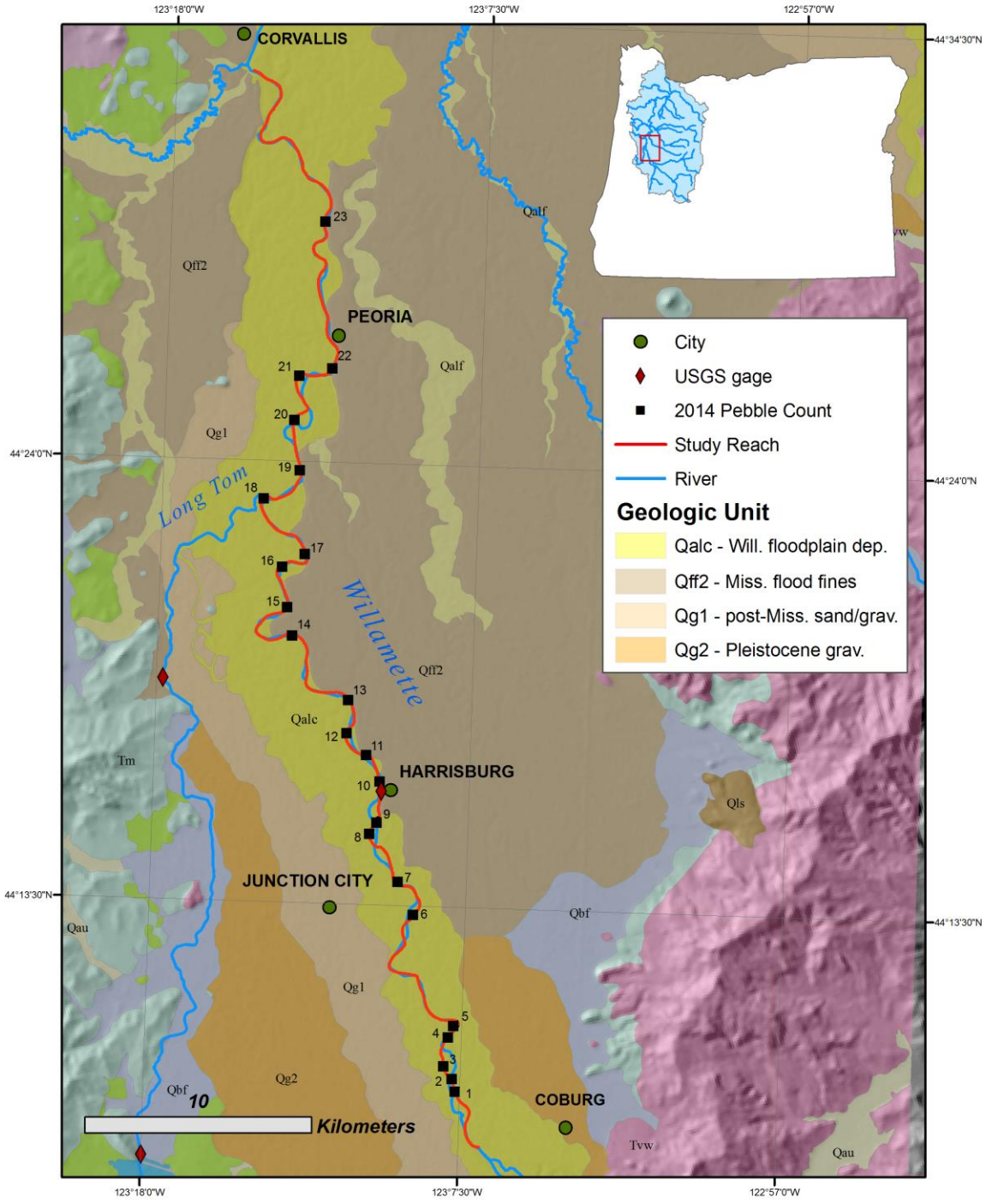

Figure 2. Site map of the Upper Willamette and study segment. Pebble count locations are labeled sequentially in the downstream direction. Geologic units from O'Connor (2001).

Wallick (2006) estimated banks composed of units Qalc and Qg2 to have an erodibility of 0.91 ± 0.50 and 0.25 ± 0.27 respectively. Erodibility is a dimensionless measure of a material's tendency to erode and is obtained by dividing the bank erosion rate by the near-bank flow velocity (higher values indicate greater erosion per unit velocity). Further she estimated the erodibility of bank revetments to be 0.015 ± 0.028.

Upstream of the McKenzie confluence (upstream of the study segment), the river flows through Pleistocene gravels. There the river is narrow and single-threaded with few active gravel surfaces. Below the McKenzie confluence and upstream of the town of Harrisburg, the river flows through Holocene alluvium (Fig. 2). In this section the active channel widens and includes many secondary channels and sloughs. The river's planform wanders rapidly via lateral migration or, less commonly, avulsions. Large active gravel bars commonly line the channel and range in area from 6,000 to 20,000 m^2 (Wallick et al., 2013). The floodplain is lower in elevation and contains many relict fluvial features representative of the river's historical dynamism. Downstream of Harrisburg and upstream of Peoria, the river frequently meanders against high terraces on the right bank where it abuts Pleistocene gravels at the water line. Here the sinuosity increases and gravel deposits are more concentrated in point bar features. Downstream of Peoria the channel becomes mainly single-threaded and flows again through Pleistocene gravels. Fewer active gravel surfaces are present in this section and mature vegetation often flanks the channel.

A large portion of banks in the study segment have been protected by revetments typically composed of boulder rip-rap and protecting banks composed of Holocene alluvium. Slope decreases with longitudinal distance, ranging over an order of magnitude

from 0.002 at the upstream end to 0.0002 at the downstream end, with a mean value of 0.0008.

Historical Narrative

Along the Willamette River, a combination of anthropogenic and natural drivers have contributed to a fluvial system that is dramatically different than that of 150 years ago. Here, we construct a brief historical narrative from the literature documenting key causal processes in the settlement and post-settlement era.

The vegetation of the Willamette valley has been modified by humans for centuries, pre-dating Euro-American settlement. The first settlers characterized the landscape as an extensive patchwork of prairie and woodland that persisted from annual fires set by Native Americans (Johannessen, Davenport, Millet, & McWilliams, 1971). Settlers brought with them agriculture, livestock and forestry. Settlement forced out native populations and ended the practice of burning. Today, agriculture (mostly large-scale grass seed production and pastureland) accounts for 43% of the valley floor while urban and rural development accounts for 11% (Hulse et al., 2007). Riparian forest communities are comprised mostly of black cottonwood and willows (Fierke & Kauffman, 2006). These habitats display complex successional patterns that are intimately linked to the development of floodplain surfaces (Dykaar & Wigington, 2000).

Efforts to improve navigability began in the 1870's. The U.S. Army Corps of Engineers (USACE) worked to close side channels and sloughs for the purpose of consolidating the river's flow. Navigability was also improved through considerable dredging and immense removal of large wood from the channel (Benner & Sedell, 1997).

After 1900, more of the valley bottom was converted for agriculture. This contributed to the closing of more side-channels and the deforestation of wooded areas. Around the same time, banks began to be stabilized such that 45% of the river's banks between the McKenzie confluence and Harrisburg were stabilized with revetments by 1995 (Wallick et al., 2007).

Beginning in the early 1940's and ending in the late 1960's, 13 medium size dams were constructed by the U.S. Army Corps of Engineers on the tributaries of the Willamette. This series of dams constitutes the Willamette Valley Project. Dams were built primarily for the purpose of flood control and navigation, although many also generate power and are used for recreation today. Between 1950 and 1995, a large number of privately owned dams were constructed mainly for irrigation purposes. Private dams and non-federal unclassified dams account for 86% of the 371 dams total in the Willamette Basin. Private dams impound a small amount of water compared to USACE dams (D. Hulse et al., 2002).

Several large floods in the 19th century were significant for the river's evolution. Large magnitude floods in 1861, 1881 and 1890 led to major avulsions, channel widening and loss of sinuosity (Wallick et al., 2007). This morphology is hypothesized to have been a natural end-member of multi-decadal cycles in which the river's sinuosity was 'reset' from large floods. However, natural recovery from these large events was constrained by development along the Willamette and the river was never fully able to re-develop a sinuous planform (Wallick et al., 2007).

The cumulative effect of the narrative described above has been a significant reduction in the geomorphic complexity of the Upper Willamette. The following account from 1875 reflects the historical dynamic and complex nature of the river:

> Each year new channels were opened, old ones closed; new chutes cut, old ones obstructed by masses of drifts; sloughs became the main bed while the latter assumed the characteristics of the former; extensive rafts are piled up by one freshet only to be displaced by a succeeding one; the formation of islands and bars is in constant progress… ("Annual Reports of Chief of Engineers for the year 1875, Part II," 1875).

This quote paints a picture dramatically different from modern conditions. Several studies have quantified simplification in geomorphic morphology. The total length of the channel between the McKenzie River confluence and Harrisburg was reduced by 60 to 70% between the 1850s and 1960s (Sedell & Froggatt, 1984). Channels that were dynamic and multi-threaded are now stable and single-threaded. Gregory (2007) found that the total island area decreased by 80% between 1850 and 1995. Bare gravel bars have diminished as vegetation is able to encroach onto surfaces that are no longer scoured in the dampened flood regime (Dykaar & Wigington, 2000). Klingeman (1973) found that the channel has incised, disconnecting it from biologically productive off-channel habitats in the floodplain. Wallick (2007) found that up to 10-20% of the river between Willamette Falls and the McKenzie confluence has narrowed between 1932 and 1995. Bed-material has coarsened due to the winnowing of fine sediment (also known as armoring) in response to the decrease in sediment supply (Klingeman, 1987).

Much of the geomorphic adjustment observed can be attributed to dams. Together, dams in the Willamette valley capture up to 27% of streamflow and trap a significant amount of sediment ("About our Willamette Valley locations," 2015). Flows greater than the 10 year flood (prior to the completion of the Willamette Valley Project) have been eliminated and flows between the 2 and 10 year floods have been substantially reduced (Fig. 3) (Risley, Wallick, Waite, & Stonewall, 2010).

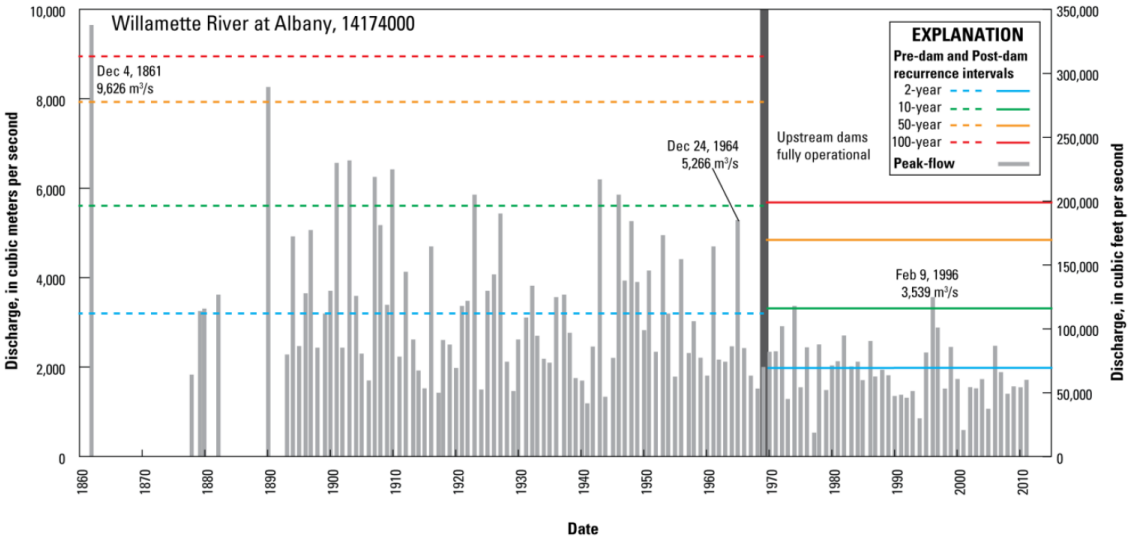

Figure 3. Peak annual discharge before and after the completion of the Willamette Valley Project at the USGS streamflow gage at Albany, Oregon. Figure from Wallick and others (2013); data from Gregory (2007).

Large floods are crucial for the transport of sediment and wood in the main channel as well as for exchanges of materials and nutrients with the floodplain. Large floods reset the succession of riparian stands (Dykaar & Wigington, 2000) and are important for the formation secondary channels (Wallick et al., 2007). Dams act as the final destination of sediment sourced upstream. Dams trap an estimated 80% of sediment of historical loads in the Middle Fork, Coast Fork and Santiam River (O'Connor et al., 2014). Water and sediment - the building blocks of fluvial dynamics – have been heavily moderated by dam operations.

Previous Studies on Sediment Transport

Previous studies by Klingeman have examined sediment dynamics in the Willamette River. A first study, published in 1973, looked at trends in channel aggradation and degradation by conducting specific gage analyses at 11 gaging stations in the Willamette Basin between water years 1935 and 1965. He found streambed degradation along the mainstem Willamette to average 1 foot per decade. He attributed degradation to gravel mining, bank stabilization and land use changes. He further concluded that dams could not be directly linked to streambed degradation (Klingeman, 1973). Wallick and others (2013) updated 7 of the specific gage analyses of Klingeman in 2013. They found that incision mostly halted following 1965. Between 1965 and 2012, gages showed greater variability in channel adjustment but little net incision. They infer this trend is due to reduced stream capacity and channel armoring.

A second study by Klingeman between 1979 and 1981 investigated the supply, movement and demand of sediment along the mainstem and its tributaries (Klingeman, 1987). He characterizes the sediment transport regime as highly dynamic and in constant adjustments to local histories and spatially discontinuous events. They found the channel to be well-armored and stable at most flow conditions, concluding that the supply of sediment from the mainstem as well as tributaries is dependent on 'appreciable flood runoff'. Bank erosion along the main channel accounts for the main source of sediment during most years. Sediment transport is discrete and local, occurring only during high flow events and traveling short distances. They infer that the majority of the sediment load consists of gravel moving from one transient storage to the next. Klingeman attempted field measurements of bed load between January and April 1980 but found that

little occurred. By the absence of transport, they suggest that the critical discharge to initialize sediment transport is greater than the mean annual flow by a factor of two or more.

In a symposium paper from 1987, Klingeman noted historical adjustments in streambed characteristics (Klingeman, 1987). He reaches two significant conclusions. Between 1969 and 1981, the streambed material coarsened overall and the downstream trend in grain size fining substantially decreased. In 1969 the median mid-channel particle size at Springfield, Salem and Portland was 55 mm, 16 mm, and 0.6 mm respectively. In the 1979-81 study, the median particle size for the combined armor layer and sub-armor layer at Harrisburg, Albany, Salem and Wilsonville was 42 mm, 14 mm 27 mm, and 19 mm. Of these, only Harrisburg falls within our study segment.

In 2014, O'Connor examined basin-scale sediment supply and transport rates for rivers in Western Oregon using empirical yield measurements and physically-derived rates of attrition (O'Connor et al., 2014). They found basin slope, lithology and lithological controls on attrition to be most significant for bed-load transport rates. They found that dams in the Willamette Basin have reduced the contributing area of sediment by 34%. Further, they estimate that the peak bed-material flux just downstream of the Santiam River confluence (about 40 km downstream of our study segment) is reduced by 64% by dams, from 199,000 t/yr to 72,000 t/yr.

CHAPTER III

METHODS

Overview

The methods undertaken in this study consist of characterizing surface grain size distributions, modeling flow and sediment transport conditions of large floods and mapping the distribution of gravel surfaces in the study segment. Grain size measurements parameterize sediment transport modeling and inform reach-scale transport dynamics. Synthetic bathymetry, coupled with topography from LiDAR, provides continuous elevation surfaces for flow and sediment transport modeling. Mapping active gravel features is used in conjunction with sediment transport modeling to analyze the balance between sediment supply and capacity. Fig. 4 provides a summary schematic relating the individual components this study's methods.

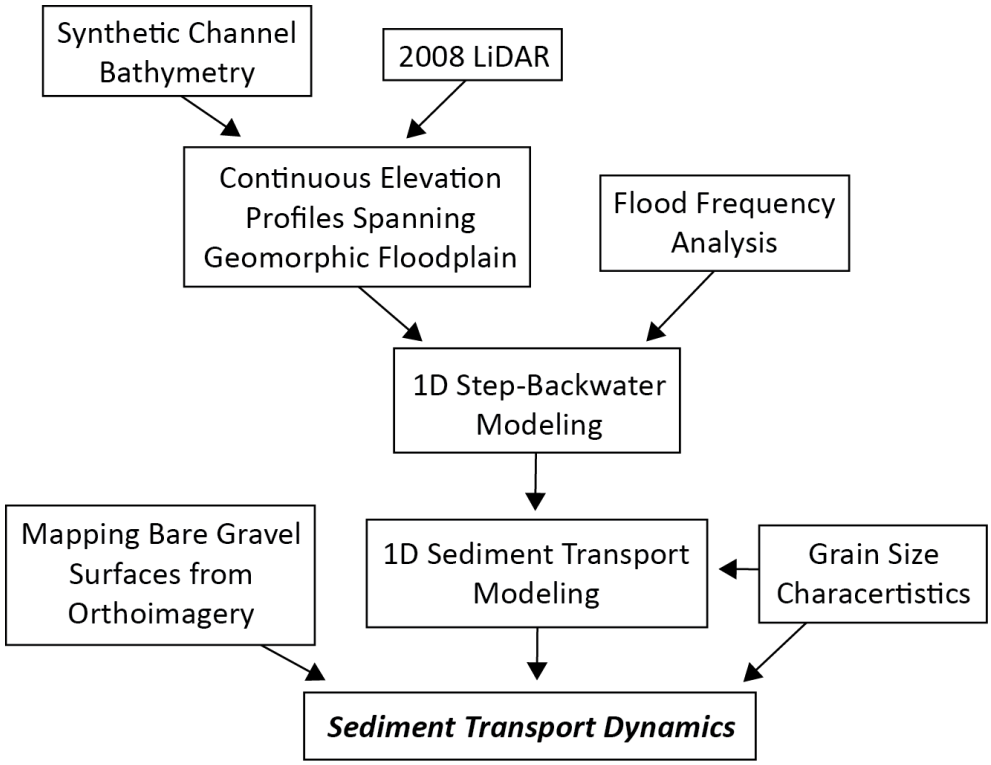

Figure 4. Schematic of methods.

Grain Size

We collected twenty-four surface grain size measurements over the summer of 2014 (Fig. 2). Sampling locations consisted mostly of point-bars but included some side bars and islands. We conducted pebble counts using a modified grid technique (Kondolf, Lisle, & Wolman, 2003). Two measuring tapes were placed 1 meter apart, aligned with the long axis of the bar (Fig. 5). Transects were located roughly at the bar centroid but adjusted to reflect bar morphology and depositional history. For example, transects would not cross a surface scoured via large wood or one that was vegetated.

Figure 5. Sampling setup for grain size measurements. Photograph taken at Bar 4.

Clasts were measured at 0.3 meter increments along a 30 meter distance of each tape for a total of 200 measurements per site. Clast grain size was measured using an aluminum gravelometer (Federal Interagency Sediment Project US SAH-97 Gravelometer). At each site, we excavated the surface layer at one point near the

upstream end of the measuring tape, placed the gravelometer inside and took a series of pictures of the subsurface. These pictures were used to qualitatively assess the level of armoring at a site. New techniques in photogrammetry and 'digital gravelometry' could be used to determine the difference in grain size distribution between the surface and sub-armor layer, though this was beyond the scope of this study. We noted imbrication structure of the surface layer when present.

Development of Cross-sections

One-dimensional flow modeling, and subsequent sediment transport modeling, required elevation data of the channel and the geomorphic floodplain. We use the same definition and geographic extent of the geomorphic floodplain as Wallick and others (2013): the area comprising the "landforms and resultant physical habitats formed chiefly by fluvial geomorphic processes active during the Holocene climatic regime of the last 10,000 years". The geomorphic floodplain is the same as unit Qalc on the study area map (Fig. 2). In order to model flood hydraulics, we extracted elevations along transects spanning the geomorphic floodplain and perpendicular to the path of water. Here, we document the work-flow of developing cross-sectional profiles for the study area.

Near-infrared LiDAR captured between 2008 and 2009 and the associated digital elevation model (DEM) provide continuous high-resolution coverage within the geomorphic floodplain of the study. These data are publically available and distributed by the Oregon Department of Geology and Mineral Industries (DOGAMI). The horizontal resolution of the DEM is 0.5 meters and the vertical accuracy is 0.04 meters RMSE (Madin, 2015). Near-infrared LiDAR reflects off the surface of water. Data over wetted

fluvial features provide elevations of the water surface itself. Other sources of information were therefore required to define bathymetry in the wetted channel.

First, we examined pre-existing bathymetric data. In 2002, the USGS surveyed bathymetric cross-sections and the longitudinal profile of the Willamette River using an Acoustic Doppler Current Profiler (ADCP) (Rounds, 2003). The applicability of these data for this study was limited because A) cross-sections were spaced 1 river mile apart; B) many cross-sections were located in areas where the planform had changed between 2002 and 2008; and C) cross-sections did not extend across the entire wetted perimeter (ADCPs have a minimum depth of measurement). Recent bathymetric surveys were collected by Mark Fonstad of the University of Oregon and the USGS Portland office, though this coincided with the later stages of this study. Other bathymetric data within the river channel was not available.

Next, we considered the method of hydraulic assisted bathymetry (HAB) (Fonstad & Marcus, 2005). HAB is a technique that uses remotely sensed imagery and hydraulic data to estimate the depth of each water pixel of the imagery. This method is only valid when the image captures light reflecting off the channel bottom. In other words, it must be possible to 'see' the channel bottom. A simple evaluation by the human-eye is usually sufficient to test this condition. It was found that the many areas of the channel-bottom could not be seen when viewing the available orthoimagery, therefore this method was excluded. Lastly, we determined that generating synthetic channel bathymetry, e.g. (Conyers & Fonstad, 2005), was the best approach for this study. This is the method we ultimately used to define channel bathymetry and is described in detail here.

Flow equations typically include a term describing the channel's geometry because it acts as a resistive force on flow. Manning's equation (eq. 1) is an empirical flow velocity equation originally developed to describe flow in open canals or pipes:

$$v = R^{2/3} \cdot S^{2/3} \cdot n^{-1} \quad (1)$$

where v is the flow velocity, R is the hydraulic radius, S is the channel slope and n is the resistance coefficient. The hydraulic radius is given by:

$$R = A \cdot P^{-1} \quad (2)$$

where A is the channel area and P is the wetted perimeter. Also, consider that velocity is related to discharge (Q) and area by:

$$v = Q \cdot A^{-1} \quad (3)$$

Substituting eq. 2 and 3 in eq. 1 and solving for area and wetted perimeter yields:

$$A^{5/3} \cdot P^{-2/3} = Q \cdot n \cdot S^{-1/2} \quad (4)$$

If Q, n and S are known, eq. 4 can be solved for the ratio between area and wetted perimeter of the channel. Additionally, area and the wetted perimeter can be found if the

channel width is known and the channel shape has the property that area and wetted perimeter area is dependent on the channel width.

We determined this method to be the best approximation of bathymetry within the wetted channel given the limitations discussed above. Four channel models (shapes) were developed concurrently: rectangle, triangle, trapezoid and parabola. The sides of the trapezoidal channels have a rise:run ratio of 2:1. In the case of split channel flow, the depth of each channel scales to its width. The definitions for the area and wetted perimeter of four channel shapes are listed in Table 1. Notice that all of these parameters are solely a function of width and depth (excepting trapezoid which includes a term for bank slope). These four channel models were selected for their prevalence in river engineering and their potential applicability to the Willamette River. The reason for developing multiple channel models is twofold: 1) There is no a-priori knowledge for which channel shape best approximates natural conditions, and 2) Multiple channel shapes allowed us to test model sensitivity to channel shape.

Transects were drawn prior to developing channel bathymetry. First, generalized flow paths were digitized for the main channel and overbank areas. Five-hundred and twelve transects were constructed orthogonal to the flow paths throughout the study segment (a spacing of roughly 130 meters). Transects were digitized using a method commonly known as ‘dog-legging’ in which transects are drawn in segments intended to be orthogonal to flow paths in the floodplain. Dog-legging also avoids transect overlap in areas of high river curvature. We considered the longitudinal spacing of transects to provide sufficient precision in characterizing variable flow conditions in the floodplain

and channel. Lastly we adjusted the longitudinal position of transects locally to reflect the diversity of channel morphology and to intersect the USGS gage at Harrisburg.

Estimates of discharge, slope and Manning's roughness coefficient were required for each transect in order to develop bathymetry in the channel. What follows is a discussion of how each variable was estimated.

Table 1. Equations for calculating the area and wetted perimeter of the four channel shapes, where A is the channel area, P is the wetted perimeter, w is the wetted width, d_{max} is the maximum channel depth and θ is the bank slope.

Shape	Area	Wetted Perimeter
Rectangle	$A = w \cdot d_{max}$	$P = 2 \cdot w + d_{max}$
Triangle	$A = {}^{1}/_{2} \cdot w \cdot d_{max}$	$P = 2 \cdot \sqrt{{}^{1}/_{2} \cdot w^2 + d^2}$
Trapezoid	$A = \frac{{d_{max}}^2}{\tan(\theta)} + d_{max} \cdot \left(w - \left(2 \cdot \frac{d_{max}}{\tan(\theta)}\right)\right)$	$P = 2 \cdot {d_{max}}^2 \frac{2 \cdot {d_{max}}^2}{\sin(\theta)} + \left(w - 2 \cdot \frac{d_{max}}{\tan(\theta)}\right)$
Parabola	$A = {}^{2}/_{3} \cdot w \cdot d_{max}$	$f = \frac{w^2 \cdot d_{max}}{16}$ $h = \frac{w}{4}$ $q = \sqrt{f^2 + h^2}$ $P = 2 \cdot \frac{q}{f} + f \cdot \log\left(\frac{h+q}{f}\right)$

Discharge (Q)

The LiDAR elevation surface within the study segment was captured on different days in accordance with the flight schedule. At each transect it was therefore necessary to calculate discharge on the specific date of capture, as a well as for the specific location. To do this, we developed a regional rating curve for each calendar day. A regional rating curve in this study is a linear regression with drainage area as an explanatory variable of discharge (e.g. Fig. 6). Mean annual discharge rates were obtained for 7 gages nearest to the study segment in the Willamette basin (Fig. 7). These 7 gages are thought to have local hydrology adequately similar to the study segment for the purposes of a rating curve. Rating curves were made for each calendar day to capture seasonal variation in regional hydrology. The rating curves define discharge relative to the discharge at the USGS Harrisburg streamflow gage. A strong negative bias was noted in the prediction of discharge at Harrisburg during the summer months (Fig. 8).

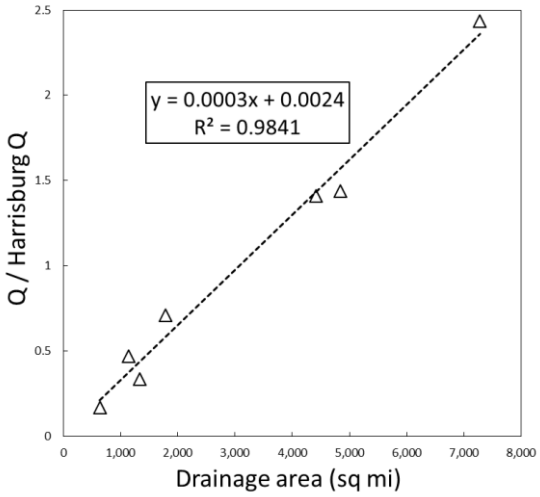

Figure 6. A regional regression curve illustrating the relationship between discharge and drainage area on a single calendar day.

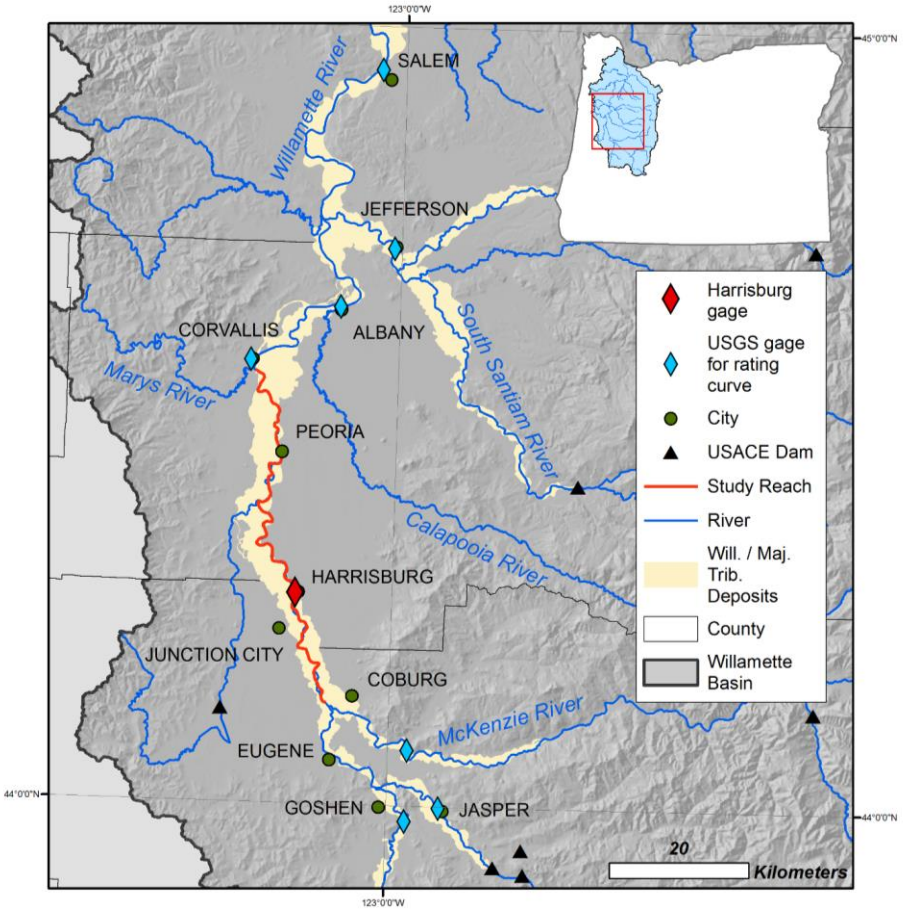

Figure 7. Map showing the location of USGS gages used in regional regression curve and the Harrisburg gage.

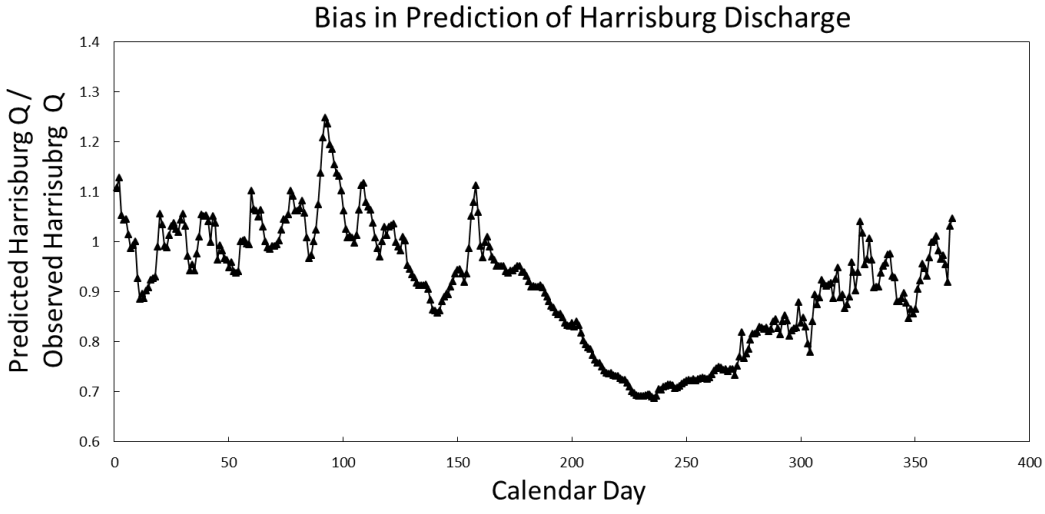

Figure 8. Bias using the regional regression curves to predict flow at Harrisburg. Note the low bias during the summer, when most of the LiDAR was captured.

A bias shift was applied such that each predictive equation passed through the point (3420, 1) where 3420 is the drainage area at Harrisburg (in square kilometers) and 1 is the discharge ratio of Harrisburg to itself. Fig. 9 shows the coefficient of determination for rating curves on each calendar day before and after the bias correction was performed. The discharge for a point along the study segment and for a specific day was calculated given the drainage area and the concurrent discharge at Harrisburg. Drainage area for each transect was found using the flow accumulation tool in ArcGIS (Fig. 10). The concurrent discharge at Harrisburg required knowing the day of LiDAR capture at each transect. Initially we examined the time signatures built into the LiDAR files. However it was found that the time was in units of GPS week-second, and the GPS week was not provided.

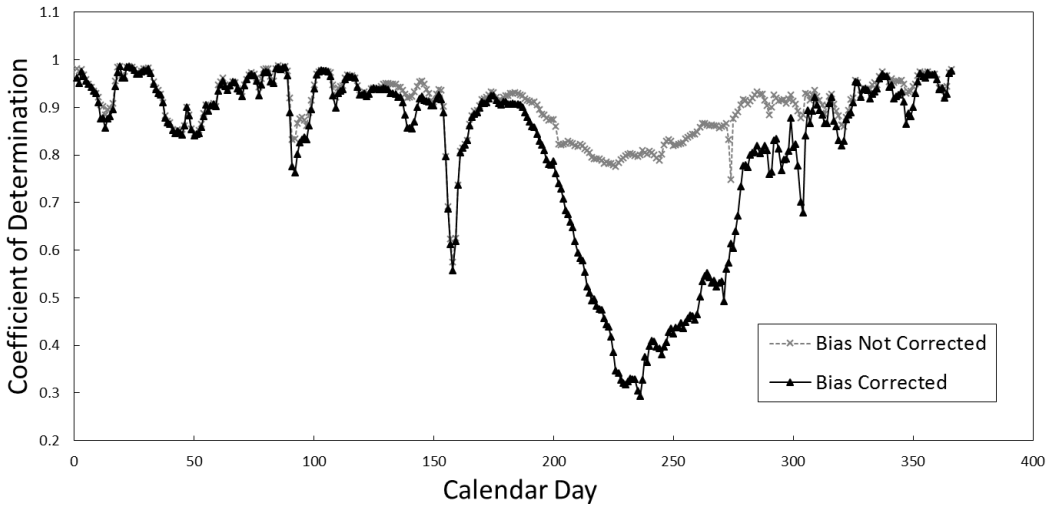

Figure 9. Change in the coefficient of determination of the regional rating curves after a bias correction was applied.

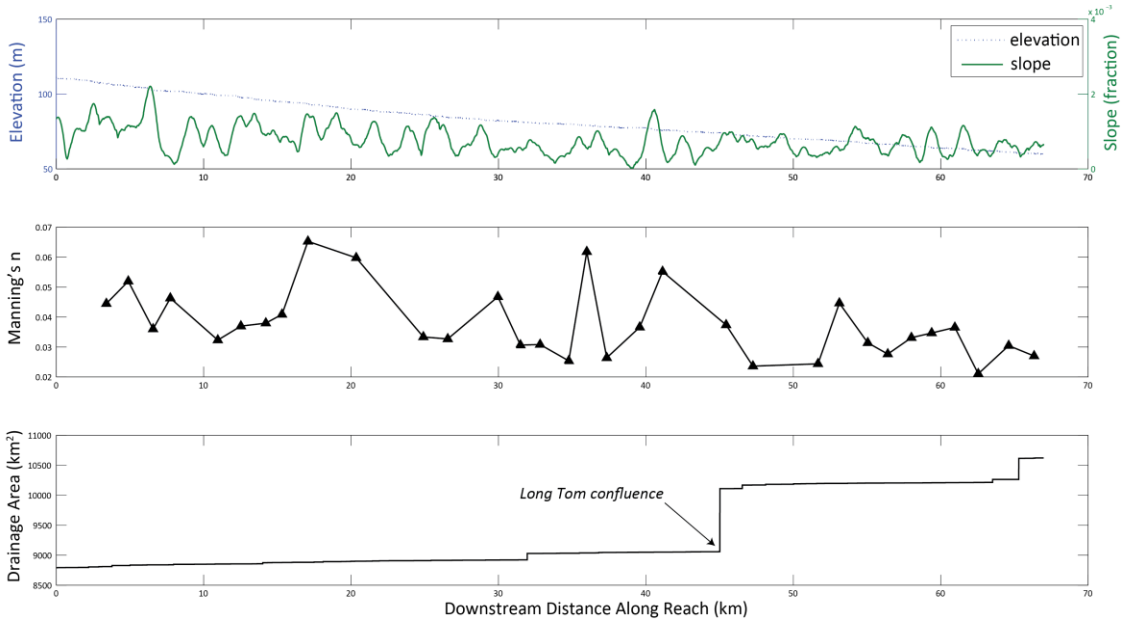

Figure 10. Longitudinal profile of drainage area, Manning's n and slope for the study segment. Downstream distance increases left to right.

Instead, time of capture was found using other specifications of the LiDAR capture. DOGAMI provided time stamped geo-referenced flight lines (Madin, 2014). The average flying elevation was 900 meters and the scan angle was ± 14° (Madin, 2015). Therefore the average ground swath coverage was ~224 meters. Lastly, it is important to note that during processing of LiDAR point data into DEMs, the lowest point was used when multiple points overlapped over a water surface (I. Madin, personal communication, October 21, 2014). A simple algorithm determined the date of LiDAR capture at a transect based on the center point's position relative to flight swaths and the Harrisburg hydrograph concurrent with those flight lines. This allowed for determination of the Harrisburg discharge on the day of LiDAR capture and thus the LiDAR discharge throughout the study segment. Table 2 provides summary statistics of discharge.

Table 2. Summary statistics for calculated discharge, slope and Manning's n within the study segment.

	Q	S	n
	m^3 / s	fraction	-
Mean	157.9	0.00076	0.038
Median	152.7	0.00071	0.036
Min	147.6	0.00002	0.021
Max	176.9	0.00220	0.065
Stdev	9.4	0.00036	0.010

Slope (S)

Slope is another parameter required to generate synthetic bathymetry (eq. 4). We measured slope from the 2008 LiDAR water surface elevation along the river centerline. Slope was calculated using a 1,250 meter moving window throughout the study segment (Fig. 10.) Table 2 provides summary statistics of slope. This window size was chosen to roughly approximate the scale of active depositional features. The centerline was broken into stations spaced 5 meters apart. At each station, the slope was calculated by simple linear regression between water surface elevation and distance within the window.

Manning's Roughness Coefficient (n)

Lastly, each transect needed to be assigned a value for Manning's roughness coefficient (n) in order to solve for synthetic bathymetry at that location (eq. 4). We calculated Manning's n using a modified version of the Manning's equation in which average depth is substituted for hydraulic radius:

$$n = D_a^{2/3} \cdot S^{1/2} \cdot v^{-1} \quad (5)$$

where D_a is the cross-sectional average depth. This substitution is commonly made in wide, shallow rivers since hydraulic radius approaches average depth as the width to average depth ratio goes to positive infinity.

Average depth, slope and velocity were sourced from the 2002 USGS ADCP bathymetric survey. We calculated average depth by averaging all depth measurements at a cross-section. There were 41 total cross-sections within the study segment though 6 were excluded for quality purposes. We used the 2008 LiDAR water surface slope as the slope estimate. Velocity was provided in the report accompanying 2002 USGS bathymetric data (Rounds, 2003). Table 2 and Fig. 10 display results for the roughness coefficient. We applied a linear interpolation between values and assigned a Manning's n value to each model transect based on downstream distance.

Finalizing Channel Bathymetry

The elevation profile was made for each transect given values of discharge, slope and Manning's n using the method described above. We first defined the channel boundary by examining the elevation profile of each transect and marking locations where the LiDAR transitioned from a land surface to a water surface. These points were quality-tested by viewing their horizontal location in ArcGIS in relation to the bare-earth and highest-hit DEMs of the LiDAR. Following this, eq. 4 and those found in Table 1 were employed to solve for the area and wetted perimeter of the four channel shapes. The maximum depth was found numerically using the 'f-zero' function in Matlab. F-zero uses a combination of bisection, secant, and inverse quadratic interpolation methods. Elevation data were extracted in the wetted channel at three meter increments.

Finally, we merged together elevations profiles outside the LiDAR wetted channel and synthetic channel bathymetry. Geometric data for modeling in HEC-RAS was prepared using Geo-RAS, a free extension for ArcMap provided by USACE for this purpose.

Flood Frequency Analysis at Harrisburg

We conducted a flood frequency analysis for the USGS gage at Harrisburg for the 'post-dam' period in the river history (1970 – present) (Fig. 11). Peak annual streamflow was accessed from the National Water Information System (NWIS) web interface. We performed our analysis using HEC-SSP 2.0 and the 'Bulletin 17B' method ("Guidlines for Determining Flood Flow Frequency," 1981). The Bulletin 17B method assumes a log-Pearson Type III distribution of the flood frequency.

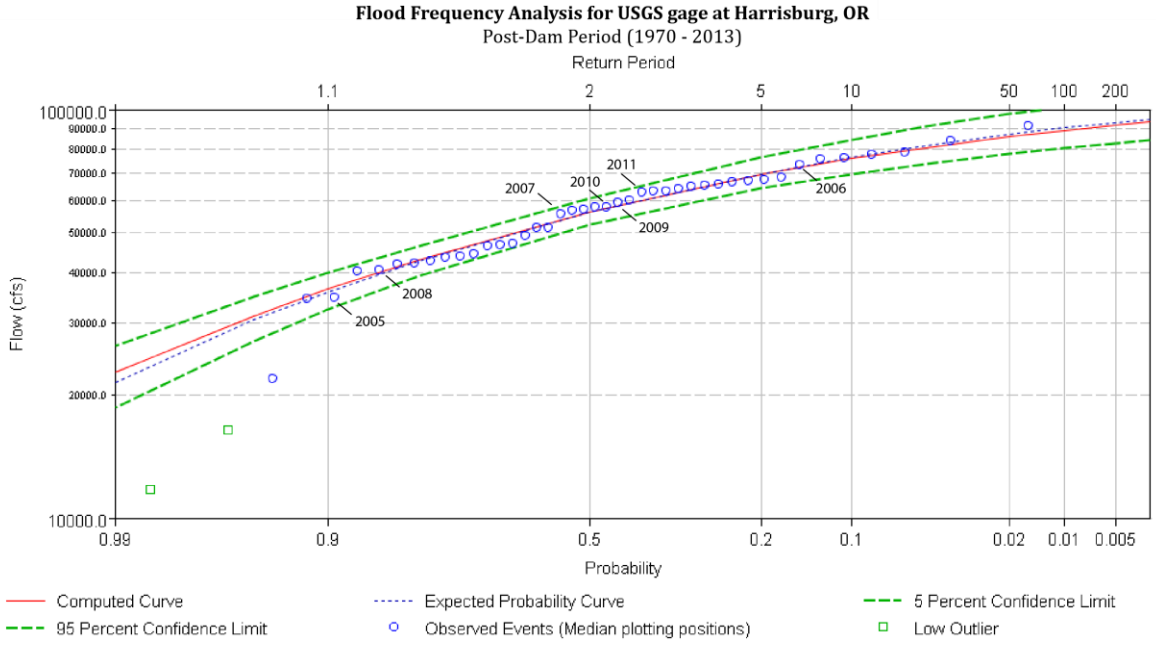

Figure 11. Flood frequency analysis for the Harrisburg gage within the post-dam period (1970 – 2013). Years between 2005 and 2011 (inclusive) are labeled. LiDAR was captured in 2008.

Step-Backwater Modeling

HEC-RAS is a hydraulic model with one and two-dimensional capabilities developed by the U.S. Army Corps of Engineers that uses a 'step-backwater' method to solve for the water surface profile (Bruner, 2010). In this study, we use HEC-RAS to model steady-state, gradually varied flow. Ten flow events were modeled spanning the 1.01 year flood to the 100 year flood (calculated in the flood frequency analysis): recurrence intervals of 1.01, 1.05, 1.11, 1.25, 2, 5, 10, 20, 50, and 100 years (Table 3).

Table 3. Recurrence interval, annual percent exceedance and discharge at Harrisburg for the 10 flow events modeled.

Recurrence Interval	Annual Percent Exceedance	Discharge at Harrisburg
years	%	m^3 / s
1.01	99	654
1.05	95	895
1.11	90	1040
1.25	80	1225
2	50	1599
5	20	1969
10	10	2148
20	5	2286
50	2	2426
100	1	2511

Hereinafter model floods are referred to by the annual percent exceedance probability: 99%, 95%, 90%, 80%, 50%, 20%, 10%, 5%, 2%, and 1%. For example, the '99% flow' means a flow event that is exceeded 99% of all years. Table 3 displays the recurrence interval annual percent exceedance and discharge at Harrisburg for the 10 flow events modeled in this study. The discharge for each cross-section and flow event was calculated using the discharge at Harrisburg and an annual regional rating curve, i.e.

we averaged all regional rating curves calculated on each calendar day as described above. Together, these data provide estimates of longitudinal variation in discharge for each flow event.

Modeling Sediment Transport

In this study, we use the terms 'sediment transport rate' and 'sediment capacity' interchangeably. The sediment transport rate refers to a volume of sediment passing through a reach per unit time. The sediment capacity refers to the total volume of sediment a reach is *able* to transport per unit time. In the case of capacity limited conditions (i.e. the supply is greater than the capacity of the river to move that sediment), the transport capacity is equal to the actual sediment transport rate. In supply limited conditions (i.e. capacity > supply) the transport capacity is greater than the actual sediment transport rate. Since supply is not known, and we did not measure sediment transport directly, the actual sediment transport rate is unknown and sediment capacity is a more appropriate term. However, we refer to our calculations as the sediment transport rate to maintain consistency with the literate on sediment transport (e.g. un-calibrated equations are still called transport equations, not capacity equations).

The sediment transport rate was calculated in the main channel for each cross-section, channel geometry and flow condition using the Wilcock & Crowe 2003 equation (Wilcock & Crowe, 2003). This is a surface-based equation that includes a similarity collapse across grain size and a hiding function based on the fraction of sand in the bulk composition. We selected this equation because it models the full distribution of the bed surface and accounts for the effect of sand content on gravel transport. Sand grains were

present at 4 of 23 sampling location in our study segment. Hydraulic modeling in HEC-RAS provided estimates for equation variables: energy gradient, hydraulic radius and channel area. Interpolated grain size distributions at each cross-section location parameterized the model as well. Using the Wilcock and Crowe 2003 equation, we calculated a dimensionless and dimensional sediment transport rate for each cross section and flow event.

Change in Gravel Bar Area

We mapped bare gravel along the main-stem for the 2005, 2006, 2009 and 2011 water years (WY). The distribution of bare gravel surfaces reflects the relative balance between erosional, depositional and vegetative processes. The purpose of mapping gravel surfaces is to determine where net deposition exceeds net erosion plus vegetative encroachment, and vice versa. The distribution of gravel provides an independent and unique metric of the sediment transport regime apart from sediment transport rates.

Mapping was performed by digitizing surfaces in ArcGIS using NAIP imagery. NAIP (National Agriculture Imagery Program) is run by the U.S. Department of Agriculture and acquires aerial imagery during the growing season (July and August in the Willamette Valley). NAIP imagery is free to access. In Oregon, the NAIP program provides color orthoimagery with extensive spatial coverage and is flown more or less every other year. A summary of the NAIP imagery we used in this study is provided in Table 4. Bare gravel was defined to be gravel with minimal vegetative cover, or vegetative cover reflecting less than one year of vegetative growth.

Table 4. Summary data for the four NAIP imagery water years used to map bare gravel bar area within the study segment.

	2005	2006	2009	2011
Format	Orthophotograph	Orthophotograph	Orthophotograph	Orthophotograph
Date of Capture	7/18/05	8/11/06	7/14/09	7/1/11
Harrisburg Q on date (m^3/s)	141	135	133	198
Resolution (m)	0.43	2	1	1
Original Source	NAIP	NAIP	NAIP	NAIP

Consideration was given to error associated with digitizing bare gravel features. Error in gravel bar area is sourced from the imagery, physical conditions at the time of capture, and human error associated with the digitization process. Rectification was performed by NAIP and the associated error is not known but is likely small in relation to the size of the gravel bars digitized. Light conditions of the photography varied from year to year and likely lead to errors in delineating bare gravel surfaces as the density and bio-volume of vegetation (especially sparse vegetation) can appear different under different light. The largest error in mapping gravel bars stems from different flow conditions at the time of capture. Discharge is directly related to stage and thus controls the inundation of gravel surfaces. The Harrisburg gage discharge at time of capture for 2005, 2006, 2009 and 2011 was 141 m^3/s, 135 m^3/s, 133 m^3/s and 198 m^3/s respectively (Table 4). For the purposes of measuring absolute change in gravel area, the combined error of the imagery, lighting conditions and discharge was considered acceptable for water years 2005, 2006 and 2009. The year 2011 was included for assessing areas where gravel surfaces are consistently not present.

CHAPTER IV

RESULTS

Grain Surface Characterization

The study segment mean for the D_{16}, D_{50} and D_{84} grain sizes is 18.3 mm, 32.3 mm and 53.8 mm respectively. Table 5 provides segment summary statistics for the D_{16}, D_{50} and D_{84} grain sizes. Values of D_{16}, D_{50} and D_{84} are plotted against downstream distance in Fig. 12. The cumulative frequency distribution of all sample locations is shown in Fig. 13. For convenience, grain sizes in mm are also log-transformed to the Ψ scale; the value of Ψ is given by the equation:

$$\Psi = \frac{\log D}{\log 2} \tag{6}$$

where D is the grain size diameter in millimeters. We calculated a simple linear regression for each grain size (mm) with distance downstream as an explanatory variable. The slope and coefficient of determination (R^2) are displayed in Table 5. All three grain sizes fine gently in the downstream direction (low negative slope values) and downstream distance explains little of the variability (low R^2 values). The D_{84} grain size fines at the greatest rate downstream (0.29 mm per kilometer), followed by the D_{50} (0.13 mm per kilometer) and the D_{16} (0.11 mm per kilometer). Grain sizes weakly to moderately correlate with distance downstream (R values around -0.30). P-values are high (especially for the D_{50}, P = 0.20) but the alternative hypothesis is very plausible (that grains fine downstream), and therefore we take the true error rate to be low. In other words, we think there is a weak, but real, relationship between grain size and distance downstream.

Table 5. (A) Summary statistics for the characteristic grain sizes; (B) slope and coefficient of determination (R^2) of a linear regression between grain size (mm) and distance downstream. See Fig. 12 for grain sizes plotted against downstream distance.

(A)	Percent Grain Size		
	D_{16}	D_{50}	D_{84}
	mm	mm	mm
Mean	18.3	32.3	53.8
Median	17.5	32.6	55.3
Min	11.6	20.3	33.1
Max	27.5	46.3	84.9
Stdev	4.8	7.6	14.2

(B)	D_{16}	D_{50}	D_{84}
Slope (mm / km)	-0.11	-0.13	-0.29
R^2	0.15	0.08	0.11
R	-0.38	-0.27	-0.34
P	0.07	0.20	0.11

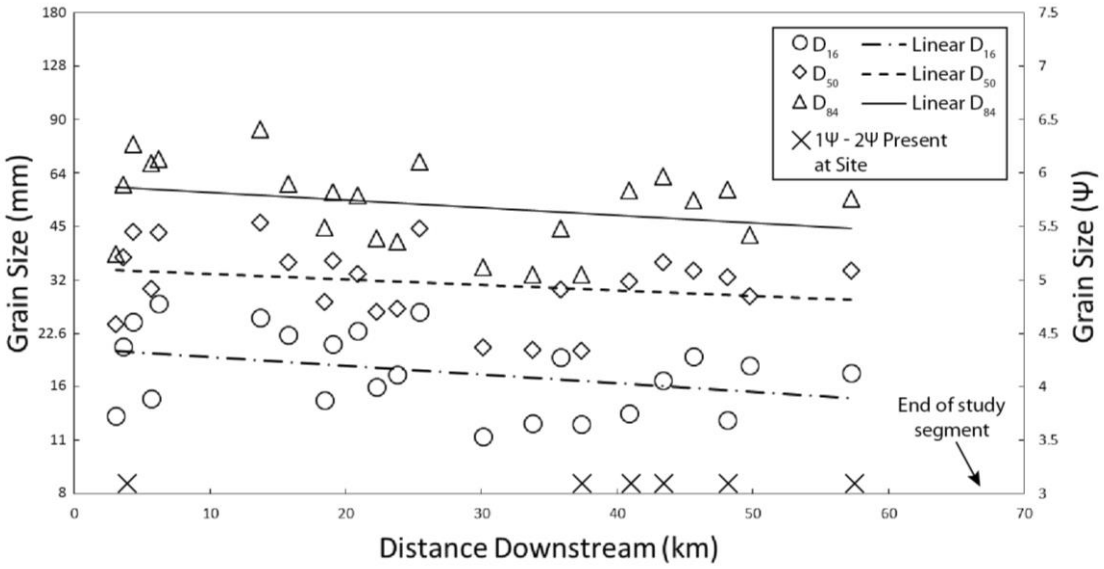

Figure 12. Downstream distribution of D_{16}, D_{50} and D_{84} grain sizes. Grain size is plotted on the left y-axis in mm and on the right y-axis by the Ψ scale. Sampling locations containing either granules or sand (1Ψ - 2Ψ) are marked with an 'X'.

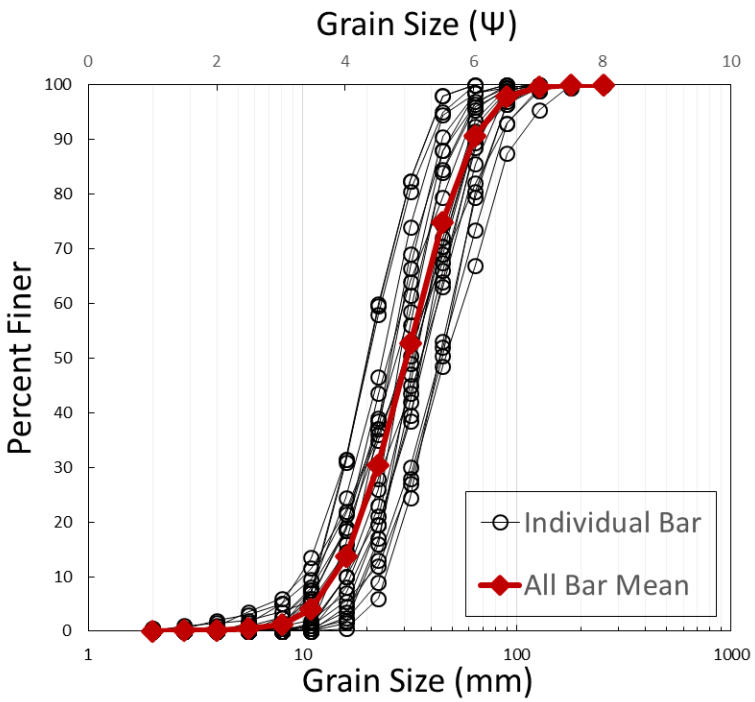

Figure 13. Cumulative frequency distribution of grain sizes for all sampling locations.

Sample locations beginning at site 17 (river kilometer 37) and downstream show a higher abundance of fines (1Ψ – 2Ψ) (Fig. 12). The Long Tom River joins the mainstem after site 18 and may be a source of fine material. Another explanation is that sampling personal changed between bar 16 and 17, and thus the increase in fines is attributable to individual sampling bias in clast selection.

The D_{84} grain size has the greatest variability (standard deviation of 14.2 mm, range of 51.8 mm) followed by the D_{50} grain size (standard deviation of 7.6 mm, range of 26.0 mm), followed by the D_{16} grain size (standard deviation of 4.8 mm, range of 15.9 mm). Larger grains therefore display greater variability than finer grains.

We noted some degree of armoring of the surface layer at all sampling locations (e.g. Fig. 14). We also observed structural imbrication of the surface layer at around ¼ of all sampling locations (e.g. Fig. 15).

Figure 14. Heavy armoring is ubiquitous along gravel bars in the Upper Willamette. This photo depicts the difference in clast size between the surface and subsurface at Bar 3.

Figure 15. Imbrication of the surface layer at Bar 2.

We compared our D_{50} grainsize measurements to historical D_{50} values listed in Klingeman (1987), using the SLICES framework (D. Hulse et al., 2002). It's not completely clear how Klingeman's data differ in sampling metholodgy (e.g. were fines included in the calculation of D_{50}?). SLICES is a floodplain centric coordinate system and thus allows us to track changes across time (whereas a river centric coordinate system is constantly changing). Table 6 and Fig. 16 display the results of this analysis. Measurements from 1969 are of the bed surface in the mid-channel. Measurements from 1979 – 1981 are composit samples of the armor layer and subarmor layer taken across the width of the channel. We calculated a simple linear regression for each data set. It is important to note that the 1969 data set consists of only 3 samples and the 1979 – 1981 data set consists of only 4. The D_{50} grain size in 1969 fines at the fastest rate (0.26 mm per floodplain km). The rate decreased by over half between 1979 – 1981 to 0.12 mm per floodplain km. Our measurements taken in 2014 are in the middle of these two though more closely alligned with the 1979-1981 rate (0.19 mm per floodplain km). The 1969 and 1979 – 1981 data display a strong positive correlation between floodlpain km and grain size ($R = 0.98$ and 0.60 respectively). Our measurements have a weak positive correlation to floodplain km ($R = 0.08$). P-values for 1969 and 2014 are relatively low ($P = 0.13$ and 0.19 respectively) in comparison to 1979 – 1981 ($P = 0.40$).

Table 6. Statistics related to simple linear regression between D_{50} grain size and floodplain kilometer for data collected in 1969, 1979 – 1981 and 2014 (Klingeman, 1987). Note that distance downstream increases with decreasing floodplain kilometer. See Fig. 16 for grain sizes plotted against floodplain kilometer.

	1969	**1979 - '81**	**2014**
	D_{50}	**D_{50}**	**D_{50}**
n	3	4	23
Slope (mm / km)	0.26	0.12	0.19
R^2	0.96	0.36	0.08
R	0.98	0.60	0.28
P	0.13	0.40	0.19

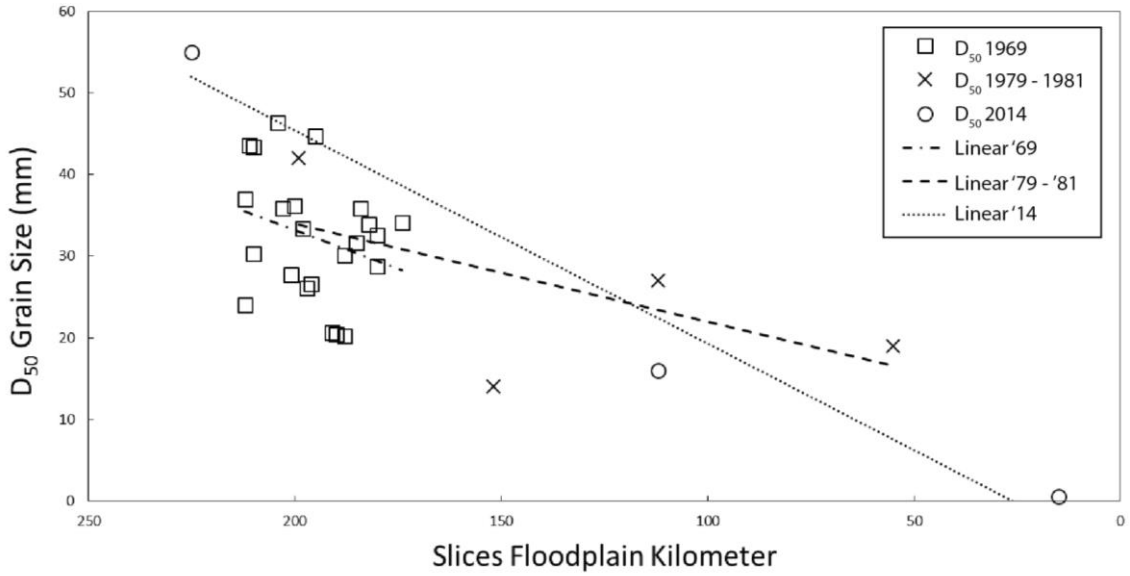

Figure 16. D_{50} measurements as listed in Klingeman (1987) along with measurements recorded in the summer of 2014. See Table 6 for statistics related to linear regression.

Channel Bathymetry

Synthetic channel bathymetry was developed using a minimal number of river variables: discharge, slope and Manning's n (Table 2). The study segment average discharge at the time of LiDAR capture is 158 m^3/s. The study segment average slope of the LiDAR water surface is 0.00076. The study segment average Manning's n value is 0.038. A Matlab code was successfully employed to automate generation of below-water bathymetry using the Manning's equation method. Four different channel geometries were developed concurrently: rectangle, triangle, trapezoid (banks of 2:1, rise:run) and parabola. Study segment average width, area, maximum depth and wetted perimeter are displayed in Table 7. Intuitively, area and the wetted perimeter decrease with the 'smoothness' of the channel shape. Differences in area are less than 5%. Fig. 17 provides an oblique perspective on a series of parabolic cross-sections created with this method. Fig. 18 shows the differences between bathymetry types at one example transect.

Table 7. Reach average geometric properties for the different synthetic channel bathymetry types.

	Rectangle	Triangle	Trapezoid	Parabola
Mean Width (m)	101.8	101.8	101.8	101.8
Mean Area (m^2)	167.0	164.7	165.8	164.4
Mean Max Depth (m)	1.7	3.4	1.7	2.5
Mean Wetted Perimeter (m)	108.2	104.9	106.5	104.6

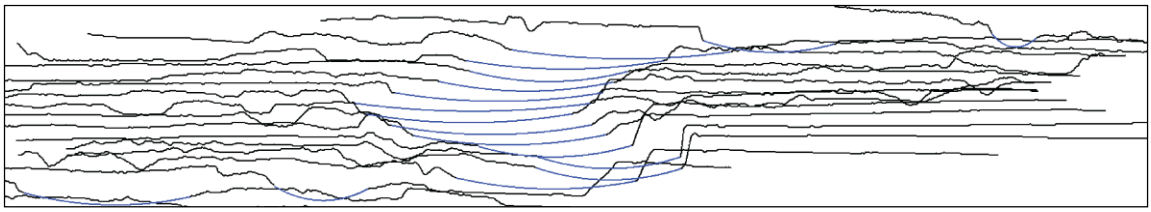

Figure 17. Oblique perspective on parabolic cross-sections developed using the Manning's method. LiDAR topography is shown in black and the synthetic bathymetry is shown in blue.

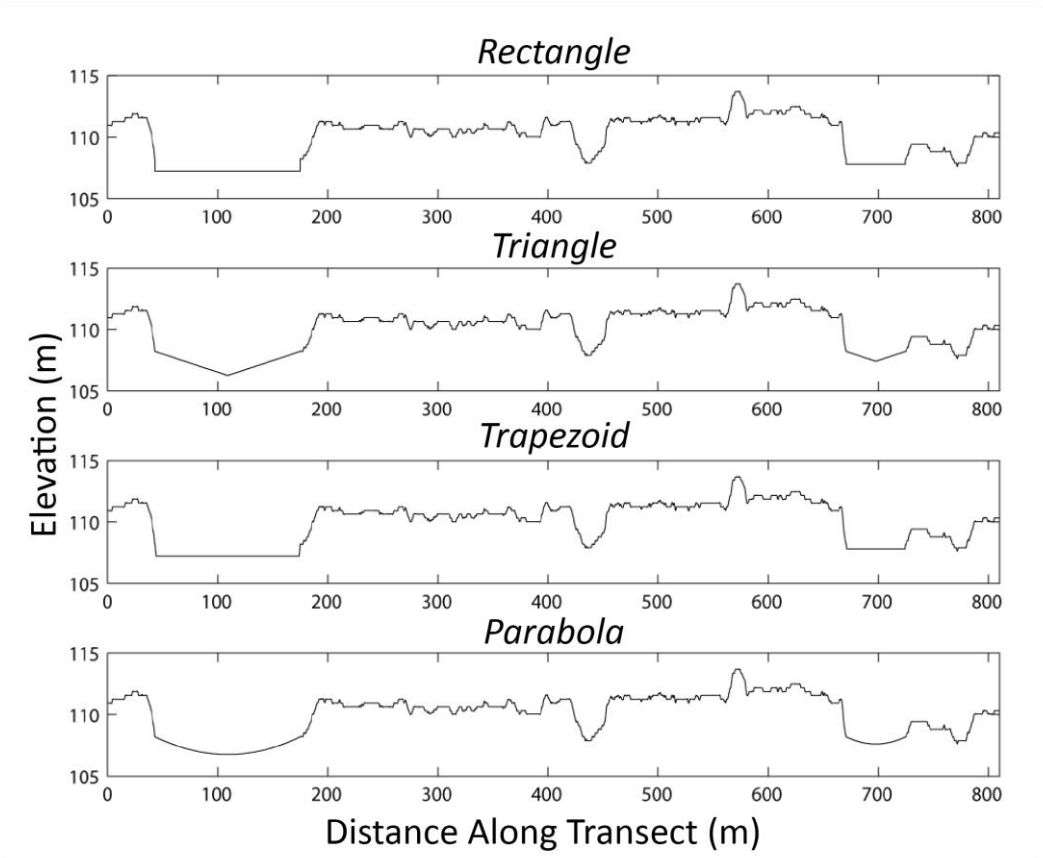

Figure 18. Example cross-section with the four types of synthetic bathymetry shown. Notice there is split channel flow (one channel centered at 100 m and a smaller one centered at 700 m).

Step-Backwater Modeling

The performance of the HEC-RAS model was assessed by comparing the rating curve of the USGS stream flow gage at Harrisburg to the model rating curve at the same location (Fig. 19). The majority of stream flow observations at the Harrisburg gage fall below the 99% annual flow exceedance (note that the lowest flow modeled was the 99% annual flow exceedance). In this domain of the rating curve (below 500 m^3/s), interpolation of model stage appears to capture the observed relationship between stage and discharge. The model does not do well at flows equal or greater to the 99% annual flow exceedance. Above this point the model predicts a stage around 1.5 meters greater than observations. Streamflow measurements do not exist for flows greater than 1,100 m^3/s, roughly the 90% annual exceedance probability.

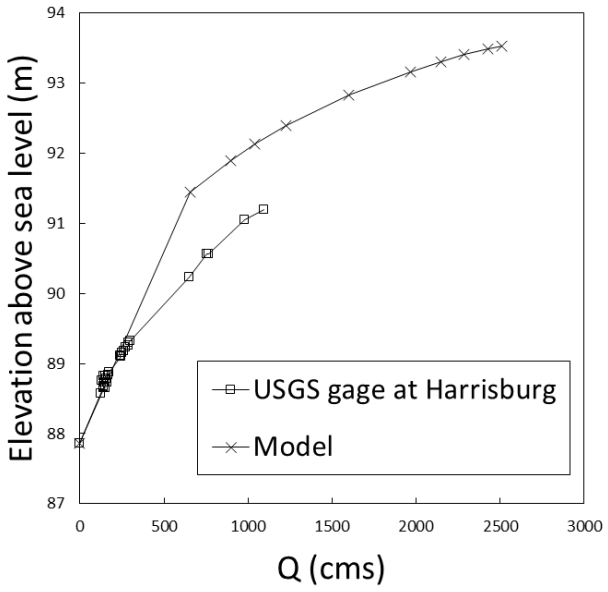

Figure 19. Comparison of model rating curve at Harrisburg to actual rating curve from Harrisburg gage

Energy gradient slope, channel area and channel hydraulic radius were required for modeling sediment transport. Summary statistics of these variables for the ten model flows is presented in Table 8. Mean area and mean hydraulic radius increase with increasing flow magnitude. The greatest increase occurs between the 99% and 80% annual percent exceedance flows, indication a transition between channelized and overbank flow. Mean energy gradient slope decreases slightly with increasing flow magnitude (from 0.00074 to 0.00071) and the standard deviation increases slightly (from 0.00042 to 0.00044). This indicates that the energy gradient profile gets flatter at higher flows but is more punctuated by finer-scale variability. Longitudinal profiles of model energy gradients are plotted in Fig. 20. As the flow rate increases, the model water surface elevations approaches critical flow depth along several sections of the river (not shown), though critical flow did not occur at any cross-section or flow.

Table 8. Summary statistics for the energy gradient, channel area, and channel hydraulic radius calculated across the study segment.

			Annual Percent Exceedence (%)									
			99	95	90	80	50	20	10	5	2	1
Energy Gradient	fraction	*Mean*	0.00074	0.00073	0.00073	0.00073	0.00072	0.00072	0.00072	0.00072	0.00071	0.00071
		Median	0.00069	0.00068	0.00067	0.00066	0.00066	0.00067	0.00066	0.00066	0.00065	0.00065
		Min	0.00008	0.00007	0.00006	0.00004	0.00004	0.00003	0.00003	0.00003	0.00004	0.00004
		Max	0.00289	0.00269	0.00280	0.00284	0.00256	0.00267	0.00269	0.00266	0.00281	0.00282
		Stdev	0.00043	0.00042	0.00042	0.00042	0.00043	0.00043	0.00043	0.00043	0.00044	0.00044
Area	m^2	*Mean*	394.4	462.7	496.1	533.5	594.8	643.1	662.8	677.1	690.9	698.5
		Median	379.1	436.6	468.8	504.2	560.3	607.0	626.5	637.9	650.6	657.8
		Min	159.0	184.7	195.0	207.5	228.6	244.9	251.2	255.8	261.2	263.6
		Max	881.8	1086.9	1193.5	1300.7	1462.2	1588.7	1639.4	1680.7	1714.9	1734.2
		Stdev	101.7	123.7	135.3	147.7	167.0	182.6	188.8	194.0	198.8	201.3
Hydraulic Radius	m	*Mean*	2.8	3.1	3.3	3.5	3.8	4.0	4.1	4.2	4.3	4.3
		Median	2.8	3.1	3.3	3.5	3.8	4.0	4.1	4.2	4.3	4.3
		Min	1.3	1.6	1.7	1.6	1.6	1.6	1.5	1.5	1.6	1.6
		Max	5.7	6.1	6.2	6.4	6.5	6.8	7.0	7.1	7.2	7.3
		Stdev	0.6	0.7	0.7	0.7	0.8	0.9	0.9	0.9	0.9	0.9

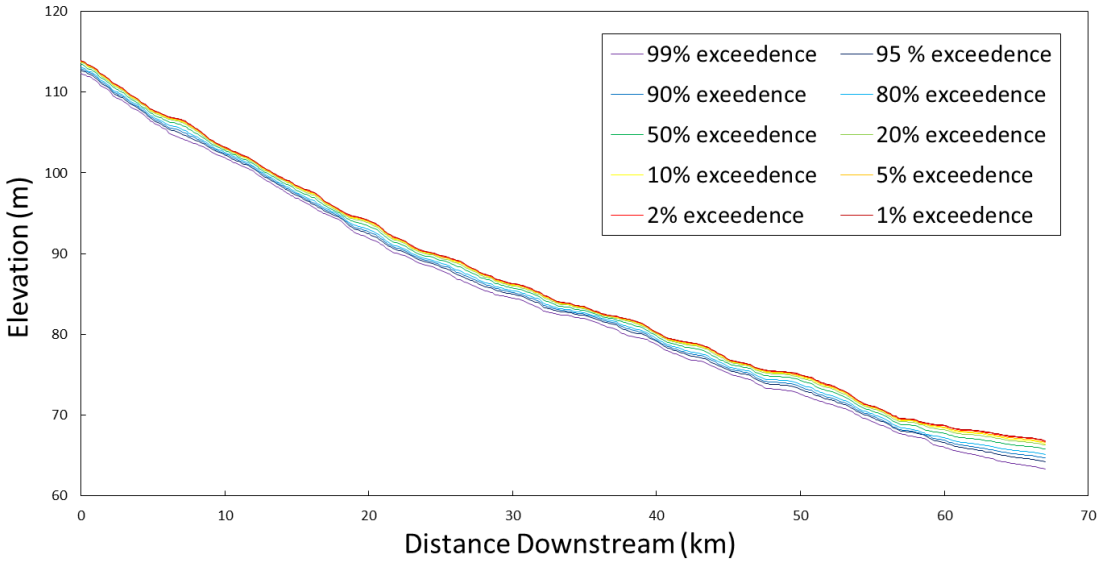

Figure 20. Longitudinal profiles of energy gradient elevation for the ten model flows.

We exported unit stream power for each transect and simulation from HEC-RAS. Unit stream power is the rate of energy dissipation against the wetted channel surface divided by the width of the channel. It is a common metric used in sediment transport studies because it scales to the power available to do work on sediment grains. Results for unit stream power are displayed in Fig. 21 and summarized in Table 9. Unit stream power shows high variability among adjacent cross-sections in the downstream direction. Values at cross-sections tend to increase at a relatively rapid rate between the 99% and 80% annual percent exceedance flows, and then gently increase with greater flow. This is attributable to a transition between channelized and overbank flow - unit stream power scales with the hydraulic radius, which increases at a greater rate below bank full discharge.

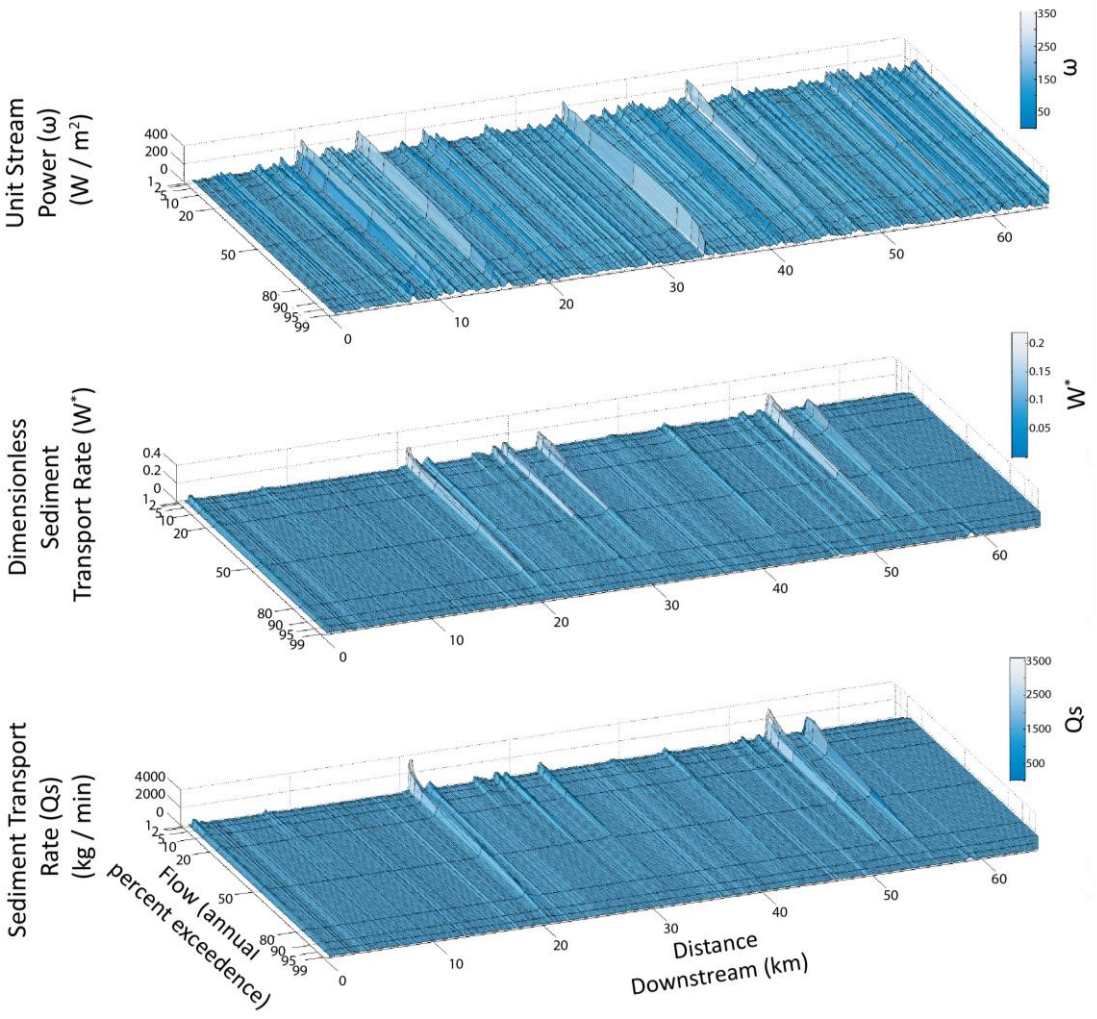

Figure 21. Unit stream power, filtered dimensionless sediment transport rate and filtered sediment transport rate. Distance downstream increases left to right on the x axis, the annual flow percent exceedance decreasing front to back on the y axis and the plotting variable increases down to up on the z axis.

Table 9. Summary statistics of unit stream power (ω), dimensionless sediment transport rate (W*), sediment transport rate (Q_s), filtered dimensionless sediment transport rate (W* filt.) and filtered sediment transport rate (Q_s filt.) calculated across the study segment.

Flow (Percent Exceedence)

	99					95				
	ω	W*	Q_s	W* filt.	Q_s filt.	ω	W*	Q_s	W* filt.	Q_s filt.
	N / m s	-	kg / min	-	kg / min	N / m s	-	kg / min	-	kg / min
Mean	2.8 x 10^+1	2.9 x 10^-3	1.9 x 10^+1	6.7 x 10^-4	2.8 x 10^+0	3.4 x 10^+1	5.9 x 10^-3	5.4 x 10^+1	1.2 x 10^-3	6.1 x 10^+0
Median	2.3 x 10^+1	4.7 x 10^-5	1.1 x 10^-1	4.9 x 10^-5	1.1 x 10^-1	2.8 x 10^+1	1.0 x 10^-4	2.7 x 10^-1	1.1 x 10^-4	3.0 x 10^-1
Min	1.0 x 10^+0	6.7 x 10^-12	5.2 x 10^-10	7.4 x 10^-9	3.5 x 10^-6	1.1 x 10^+0	1.1 x 10^-11	9.7 x 10^-10	3.5 x 10^-9	1.0 x 10^-6
Max	1.8 x 10^+2	5.0 x 10^-1	4.8 x 10^+3	3.9 x 10^-2	1.9 x 10^+2	2.7 x 10^+2	9.1 x 10^-1	1.4 x 10^+4	4.1 x 10^-2	2.1 x 10^+2
Stdev	1.9 x 10^+1	2.4 x 10^-2	2.2 x 10^+2	3.6 x 10^-3	1.7 x 10^+1	2.5 x 10^+1	4.5 x 10^-2	6.4 x 10^+2	3.7 x 10^-3	2.1 x 10^+1
	90					80				
	ω	W*	Q_s	W* filt.	Q_s filt.	ω	W*	Q_s	W* filt.	Q_s filt.
	N / m s	-	kg / min	-	kg / min	N / m s	-	kg / min	-	kg / min
Mean	3.7 x 10^+1	7.7 x 10^-3	8.1 x 10^+1	1.8 x 10^-3	9.8 x 10^+0	4.0 x 10^+1	1.0 x 10^-2	1.1 x 10^+2	3.1 x 10^-3	1.8 x 10^+1
Median	3.1 x 10^+1	1.3 x 10^-4	4.1 x 10^-1	1.5 x 10^-4	5.5 x 10^-1	3.4 x 10^+1	1.7 x 10^-4	6.4 x 10^-1	2.1 x 10^-4	8.0 x 10^-1
Min	1.2 x 10^+0	1.5 x 10^-11	1.4 x 10^-9	1.4 x 10^-9	3.6 x 10^-7	1.2 x 10^+0	1.9 x 10^-11	2.1 x 10^-9	1.0 x 10^-9	2.5 x 10^-7
Max	3.1 x 10^+2	1.0 x 10^+0	1.9 x 10^+4	3.5 x 10^-2	3.1 x 10^+2	3.5 x 10^+2	1.1 x 10^+0	2.4 x 10^+4	5.9 x 10^-2	6.2 x 10^+2
Stdev	2.8 x 10^+1	5.2 x 10^-2	8.8 x 10^+2	4.4 x 10^-3	3.0 x 10^+1	3.1 x 10^+1	6.1 x 10^-2	1.1 x 10^+3	7.5 x 10^-3	5.9 x 10^+1
	50					20				
	ω	W*	Q_s	W* filt.	Q_s filt.	ω	W*	Q_s	W* filt.	Q_s filt.
	N / m s	-	kg / min	-	kg / min	N / m s	-	kg / min	-	kg / min
Mean	4.6 x 10^+1	1.5 x 10^-2	1.7 x 10^+2	6.7 x 10^-3	4.9 x 10^+1	5.0 x 10^+1	2.0 x 10^-2	2.2 x 10^+2	9.6 x 10^-3	8.0 x 10^+1
Median	3.8 x 10^+1	2.9 x 10^-4	1.3 x 10^+0	3.0 x 10^-4	1.4 x 10^+0	4.2 x 10^+1	3.8 x 10^-4	1.8 x 10^+0	3.7 x 10^-4	1.7 x 10^+0
Min	1.5 x 10^+0	7.3 x 10^-11	1.1 x 10^-8	1.5 x 10^-9	4.0 x 10^-7	1.4 x 10^+0	1.3 x 10^-10	1.6 x 10^-8	9.8 x 10^-10	2.4 x 10^-7
Max	3.3 x 10^+2	1.1 x 10^+0	2.1 x 10^+4	9.8 x 10^-2	1.1 x 10^+3	2.8 x 10^+2	7.9 x 10^-1	1.2 x 10^+4	1.4 x 10^-1	1.9 x 10^+3
Stdev	3.6 x 10^+1	6.8 x 10^-2	1.1 x 10^+3	1.6 x 10^-2	1.6 x 10^+2	3.9 x 10^+1	6.9 x 10^-2	9.9 x 10^+2	2.4 x 10^-2	2.4 x 10^+2
	10					5				
	ω	W*	Q_s	W* filt.	Q_s filt.	ω	W*	Q_s	W* filt.	Q_s filt.
	N / m s	-	kg / min	-	kg / min	N / m s	-	kg / min	-	kg / min
Mean	5.2 x 10^+1	2.2 x 10^-2	2.7 x 10^+2	1.1 x 10^-2	9.8 x 10^+1	5.4 x 10^+1	2.3 x 10^-2	2.9 x 10^+2	1.2 x 10^-2	1.1 x 10^+2
Median	4.4 x 10^+1	4.6 x 10^-4	1.9 x 10^+0	4.6 x 10^-4	2.0 x 10^+0	4.5 x 10^+1	5.4 x 10^-4	2.3 x 10^+0	5.7 x 10^-4	2.3 x 10^+0
Min	1.6 x 10^+0	2.0 x 10^-10	2.6 x 10^-8	2.6 x 10^-9	8.1 x 10^-7	1.6 x 10^+0	2.7 x 10^-10	3.8 x 10^-8	3.8 x 10^-9	1.2 x 10^-6
Max	3.0 x 10^+2	8.6 x 10^-1	1.6 x 10^+4	1.7 x 10^-1	2.6 x 10^+3	3.1 x 10^+2	7.5 x 10^-1	1.7 x 10^+4	1.8 x 10^-1	2.7 x 10^+3
Stdev	4.2 x 10^+1	7.8 x 10^-2	1.2 x 10^+3	2.8 x 10^-2	3.1 x 10^+2	4.2 x 10^+1	7.7 x 10^-2	1.2 x 10^+3	3.0 x 10^-2	3.4 x 10^+2
	2					1				
	ω	W*	Q_s	W* filt.	Q_s filt.	ω	W*	Q_s	W* filt.	Q_s filt.
	N / m s	-	kg / min	-	kg / min	N / m s	-	kg / min	-	kg / min
Mean	5.5 x 10^+1	2.5 x 10^-2	3.3 x 10^+2	1.2 x 10^-2	1.1 x 10^+2	5.6 x 10^+1	2.6 x 10^-2	3.4 x 10^+2	1.3 x 10^-2	1.3 x 10^+2
Median	4.4 x 10^+1	6.0 x 10^-4	2.4 x 10^+0	5.8 x 10^-4	2.3 x 10^+0	4.6 x 10^+1	6.0 x 10^-4	2.5 x 10^+0	6.0 x 10^-4	2.2 x 10^+0
Min	1.7 x 10^+0	3.7 x 10^-10	5.6 x 10^-8	6.5 x 10^-9	2.3 x 10^-6	1.8 x 10^+0	4.1 x 10^-10	6.3 x 10^-8	7.2 x 10^-9	2.7 x 10^-6
Max	3.0 x 10^+2	8.3 x 10^-1	1.6 x 10^+4	1.9 x 10^-1	3.1 x 10^+3	3.1 x 10^+2	8.5 x 10^-1	1.7 x 10^+4	2.1 x 10^-1	3.5 x 10^+3
Stdev	4.4 x 10^+1	8.3 x 10^-2	1.3 x 10^+3	3.1 x 10^-2	3.6 x 10^+2	4.5 x 10^+1	8.4 x 10^-2	1.4 x 10^+3	3.3 x 10^-2	4.2 x 10^+2

Sediment Transport Rates

We calculated sediment transport rates at each transect for each of the 10 flow simulations using the Wilcock & Crowe 2003 equation. The model was parameterized using hydraulic variables output from HEC-RAS and our grain size measurements. Grain size distributions were interpolated at each cross-section location.

We examined the significance of channel shape for sediment transport rates using a Wilk's multivariate analysis of variance (with annual percent exceedance and channel shape as variables). The p-value was 0.99 and the f-score was 0.27. The null hypothesis was not rejected and sediment transport rates were concluded not to vary significantly with channel shape. The results of individual analyses of variance for all flow simulations are summarized in Table 10. This gave us confidence to analyze subsequent results using only one synthetic channel geometry (parabolic). A different channel shape could have been selected – the results state that is does not matter.

Table 10. Analysis of variance and multiple analysis of variance testing the significance of synthetic channel bathymetry type on sediment transport rates.

ANOVA

	Flow (Percent Exceedence)									
	99	95	90	80	50	20	10	5	2	1
F value	1.4 x 10^-2	1.0 x 10^-2	2.0 x 10^-2	8.7 x 10^-3	1.1 x 10^-2	4.2 x 10^-3	1.9 x 10^-3	6.1 x 10^-3	2.9 x 10^-2	9.0 x 10^-4
P value	0.90	0.92	0.89	0.93	0.92	0.95	0.97	0.94	0.86	0.98
Reject H_0	no	no	no	no	no	no	no	no	no	no

Wilk's Test

	all flows
F value	2.7E-01
P value	0.99
Reject H_0	no

Sediment transport rates (both dimensional and dimensionless) were post-processed using a median value filter. Specifically, the sediment transport rate at a cross-section was recalculated as the median value of the transport rate of the 5 upstream and 5 downstream cross-sections (a window size of 1.3 km on average). Median value filters are commonly used in digital image processing because they reduce signal noise and preserve 'edges' in the data. They are particularly useful for removing extreme values in the data because the median is largely insensitive to outliers. The rationale in applying this filter is that we believe it aids in revealing the underlying structure of the data. Sediment transport formulas (including Wilcock & Crowe) are highly non-linear. By applying a median-value filter, we sought to eliminate noise associated with this non-linearity. There is a question of how much information is lost by filtering the data. We consider this loss of information acceptable because there is great uncertainty in the raw calculation of sediment transport values. In addition to the non-linear governing equations, there are no direct measurements of sediment transport on the Upper Willamette (by us or others). Our primary goal was to analyze the relative pattern of sediment transport rates across flow magnitude and downstream distance. Note that ratios or differences can hold in spite of scaling or bias errors in the absolute values. For these reasons, we believe that filtering the sediment transport rates aids in our analysis more than it detracts from it. More will be said about this in the discussion section.

Fig. 21 shows the pattern of filtered transport rates across downstream distance and flow magnitude. Transport rate data are recorded in Table 9. Sediment transport rates (Qs) are even across downstream distance with few widely scatter peaks. Peaks in the dimensionless sediment transport rate (W*) generally correspond to those of Qs in

location, though they are greater in number and differ in the distribution of their magnitudes. Both show a longitudinal pattern that is relatively consistent across flow values, i.e. where there is a peak in the 99% annual exceedance, there is typically also a peak in the 1% annual exceedance. Values of Qs and W* increase with increasing flow magnitude. Unit stream power (ω) shows finer-scale irregularity in peaks and troughs with downstream distance. Peaks in ω do not correspond to peaks in Qs or W*. The difference between mean raw sediment transport rates and mean filtered sediment transport rates is less than an order of magnitude across most flows (Table 9). Maximum transport rate values in the study segment decrease after filtering (typically between 1 to 2 orders of magnitude) and median values increase slightly.

We calculated a flow normalized sediment transport rate at each cross-section from the filtered dimensional sediment transport rates. The purpose of calculating a flow normalized sediment transport rate is to collapse all flow series to a single characteristic metric of sediment transport in the study segment. In this way, we isolate variability in sediment transport with longitudinal distance. Here we define the flow normalized sediment transport rate as the weighted average across all flows, with weight equal annual exceedance probability:

$$\overline{Q_s} = \frac{\sum_{i=1}^{n} Q_{si} \cdot P_i}{\sum_{i=1}^{n} P_i} \tag{7}$$

where Q_s is the flow normalized sediment transport rate at a transect, and P_i is the annual exceedance probability of the ith flow event. The resulting value can be thought of as the characteristic sediment transport rate in the current flow regime (Fig. 22).

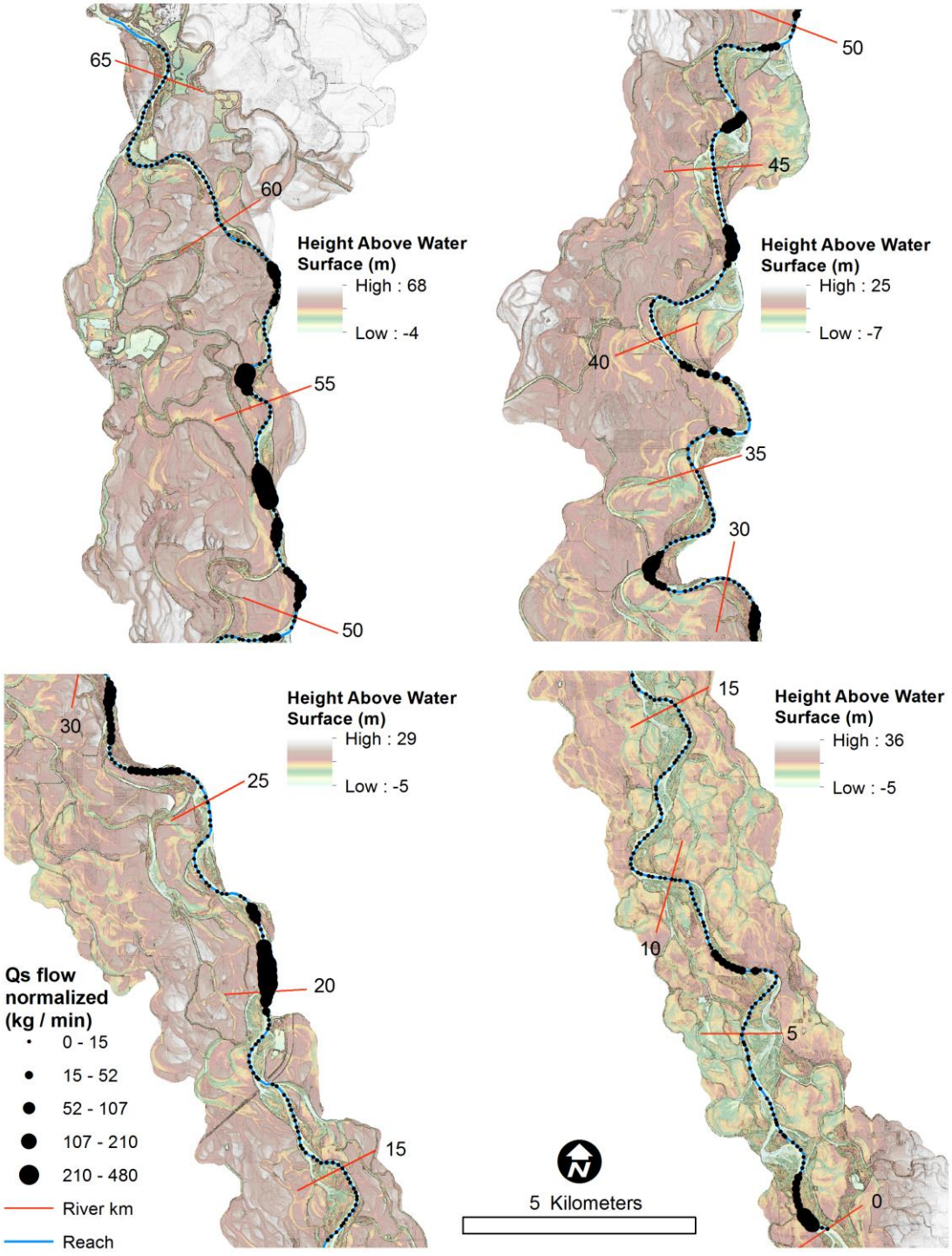

Figure 22. Flow normalized sediment transport rate mapped for the study segment. The sediment transport rate is classified using 5 classes and natural breaks. LiDAR topography colors have been adjusted in reference to the water surface elevation.

Values of $\overline{Q_s}$ are highly discrete in longitudinal space. Values in the lower section upstream of river kilometer 20 (the town of Harrisburg) are low with relatively few peaks. Downstream of this point, there are much larger peaks in the data, peaks occur more frequently and are often located at bends in the river. In the next section, we analyze the flow normalized sediment transport rate in relation to the distribution of bare gravel surfaces.

Relationship between Grain Size and Stream Power

We developed a correlation matrix between the measured $D_{16,}$ D_{50}, D_{84} grain sizes, and unit stream power for the 10 flow simulations. The purpose of this was to analyze the relationship between grain size and transport conditions. A strong correlation theoretically indicates a formative link between the flow event and the grain size (Jacobson, O'Connor, & Oguchi, 2003), and is thus indicative of which flow events are important for shaping bar morphology. Fig. 23 shows a scatter plot for each matrix component and Table 11 provides the coefficient of determination, Pearson's correlation coefficient and correlation p-value. All grain size-flow pairs were weakly correlated (low R values) and were not significant (high P-values). The D_{16} was most highly correlated with the 5% exceedance flow (0.17), D_{50} with the 90% exceedance flow (-0.12) and D_{84} with the 90% flow (-0.06). A negative correlation between grain size and stream power is not expected because competence increases with stream power, thus mobilizing larger grains. We calculated a flow normalized unit stream power value by substituting unit stream power for the sediment transport rate in eq. 7. The downstream variation in the flow normalized unit stream power is displayed in Fig 24. along with the $D_{16,}$ D_{50}, D_{84}.

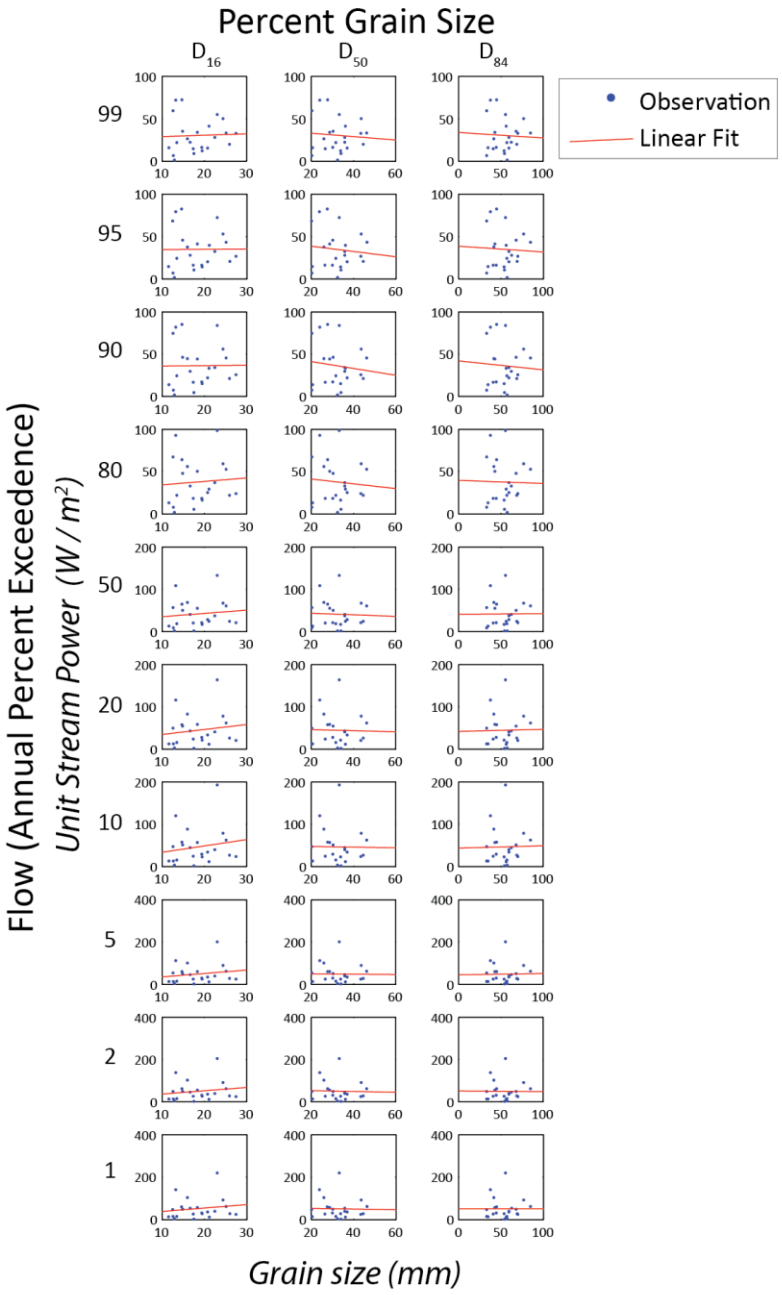

Figure 23. Three by ten scatter plot matrix corresponding to the characteristic grain sizes and the ten model flows. Each point represents the position of a grain sample location in terms of grain size and model unit stream power at the same location. Simple linear regression lines are shown in red.

Table 11. Coefficient of determination (R^2), Pearson's correlation coefficient (R) and p-value (P) for each scatter plot in Fig. 23 relating the three characteristic grain sizes and stream power of the ten model flows.

	Percent Grain Size								
	D_{16}			D_{50}			D_{84}		
Flow (Percent Exceedence)	R^2	R	P	R^2	R	P	R^2	R	P
99	0.001	0.04	0.86	0.006	-0.08	0.72	0.002	-0.05	0.84
95	0.000	0.01	0.97	0.010	-0.10	0.65	0.002	-0.04	0.85
90	0.000	0.01	0.97	0.014	-0.12	0.59	0.003	-0.06	0.79
80	0.005	0.07	0.74	0.006	-0.08	0.72	0.000	-0.02	0.93
50	0.013	0.11	0.60	0.002	-0.04	0.85	0.000	0.01	0.97
20	0.021	0.15	0.51	0.001	-0.03	0.91	0.000	0.02	0.93
10	0.028	0.17	0.45	0.000	-0.01	0.95	0.000	0.02	0.93
5	0.031	0.17	0.43	0.000	-0.01	0.96	0.000	0.02	0.93
2	0.022	0.15	0.50	0.001	-0.03	0.88	0.000	-0.01	0.97
1	0.023	0.15	0.49	0.001	-0.03	0.91	0.000	0.00	0.99

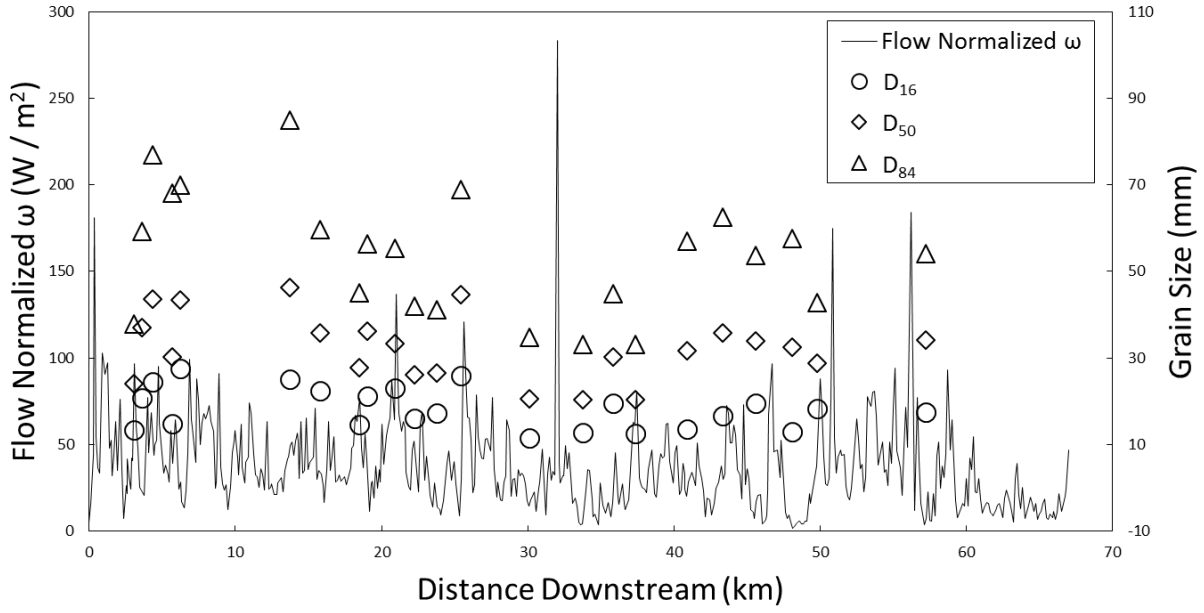

Figure 24. Downstream distribution of D_{16}, D_{50} and D_{84} grain sizes and flow normalized unit stream power. Unit stream power shows high variability among adjacent transects. No clear relationship emerges between grain size and stream power.

No clear trend in the unit stream power rate emerges from this analysis. The downstream pattern appears to be dominated by variability at scale of cross-sectional spacing. Further, visual inspection does not lead to any clear relationship between grain size and the flow normalized unit stream power. The overall poor correlation between characteristic grain sizes and stream power suggests that no one flow condition dominates bar morphology dynamics in the Upper Willamette River. In the next section, we present results for analyze the distribution of bare gravel surfaces and its relationship to the flow normalized sediment transport rate.

Change in Bare Gravel Surfaces

We digitized active gravel features from NAIP imagery for 2005, 2006, 2009 and 2011 within the study segment. Table 12 shows the change in active gravel area during this time. 2011 is not included here due to the large error resulting from high discharge values (compared to the other years) at the time of imagery capture. Gravel bar area increased between the summers of 2005 and 2006. The peak winter flow between these images was 2073 m^3/s. Gravel area subsequently decreased between the summer of 2006 and 2009. The peak flow in this time period was 1671 m^3/s occurred in the winter of 2009.

We examined the relationship between the flow normalized sediment transport rate and distribution of bare gravel surfaces. Fig. 25 plots these two variables together with gravel area on the left axis and transport rate on the right axis. The distribution of gravel surfaces is displayed for 2005, 2006, 2009 and 2011 (2011 is included here for the

purpose of locating areas with consistently low gravel, despite the error associated with discharge at the time of capture).

The data reveal that there are numerous sections of the reach that consistently have little to no gravel deposits over the 6 year period mapped between 2005 and 2011 WYs. Of these, there are four segments with practically no gravel across all years occurring near river kilometers 8, 20, 29, 40 and 52 (Fig. 25).

There is a notable relationship between the distribution of active gravel and the distribution of flow normalized sediment transport rates. There is a strong level of alignment between spikes in the flow-normalized Qs and amount of active gravel mapped between 2005 and 2011. High peaks in Qs generally correspond to areas with relatively low active gravel. Spikes in sediment transport are often seen to bracket reaches of the river with a large amount of bare gravel. Eleven pairs of this type have been identified and highlighted on Fig. 25 in gray. Several reaches of the study segment defy this pattern though they are few in number. Three exceptions stand out where there is relatively little gravel and no spike in sediment transport. These are indicated on Fig. 25 with arrows. There is one location where there is a spike in sediment transport and a relatively high amount of active gravel (also indicated on Fig. 25).

Table 12. Absolute bare gravel bar area and change in bare gravel area for NAIP imagery years 2005, 2006 and 2009.

2005 bar area	2006 bar area	2009 bar area	2005 - 2006	2006 - 2009
km^2	km^2	km^2	change (%)	change (%)
1.2	1.6	1.1	24%	-53%

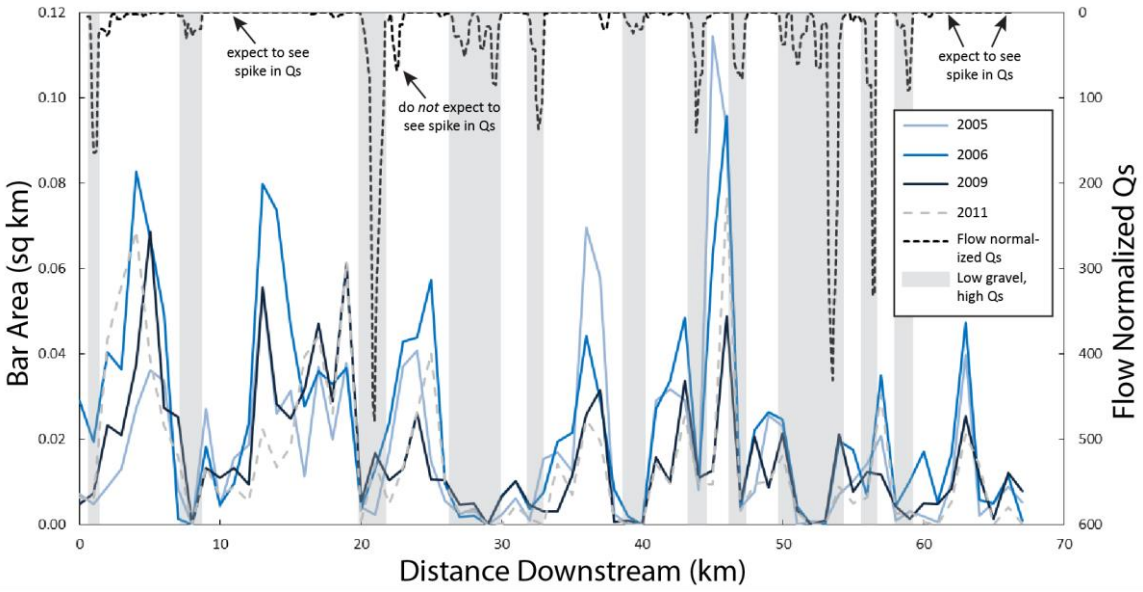

Figure 25. Downstream distribution of bare gravel surfaces for years NAIP imagery years 2005, 2006 and 2009. The flow normalized sediment transport rate is plotted as a dashed black line on the right axis. Areas highlighted in gray show low gravel bar area for the study period and high sediment transport rates. Arrows highlight sections where sediment transport rates and gravel bar area do not agree.

CHAPTER V

DISCUSSION

Grain Surface Characterization

The D_{16}, D_{50} and D_{84} all fine in the downstream direction (Fig. 12). High p-values (Table 5) indicate there is a chance that we have reached false-positive conclusions in each case. However, given the agreement across grain sizes, general fluvial theory, and previous observations of downstream fining in the Willamette, we consider downstream fining in our samples to reflect a weak, but real, relationship. We also suggest that part of the fining signal is obscured by noise associated with fine-scale variability in grain size distributions.

Clasts undergo fracture, abrasion, weathering and dissolution during transport (Reid & Dunne, 2005). Altogether, these processes lead to fining of clasts, increases in roundness and changes in particle composition as grains are transported downstream. The mechanical wear that produces grain fining is known as attrition. The supply of grains associated with the bed load decreases in the downstream direction as clasts become small enough to be transported in suspension. Selective-transport is a related process responsible for downstream fining in which larger clasts are preferentially deposited and smaller clasts are carried further downstream. Selective-transport has been shown to dominate the downstream fining of sediment in some systems, particularly alluvial rivers such as the Willamette (Miller, Szabó, Jerolmack, & Domokos, 2014; S. Rice & Church, 1998). However, both processes occur in tandem (Church, 1978) and their relative contribution to downstream fining is difficult to assess (Miller et al., 2014)

Clasts size are predicted to decay exponentially with distance downstream due to attrition, given by Sternberg's Law (Sternberg, 1875):

$$D_x = D_0 \cdot e^{(-\alpha x)} \quad (7)$$

where D_0 is the initial pebble diameter, α is empirical decay coefficient and x is the distance downstream. However, we found that grain size decays at a linear rate (Fig. 13). Further, we found that larger grains fine at a faster rate downstream. This is not predicted by Sternberg's Law since α does not scale with D_0. This may suggest that the process of attrition does not dominate the fining of the surface material. Instead, we infer that selective transport is the main process by which clast size decreases in the downstream direction.

There are several constraints on comparing our grain size data to historic measurements. First, the number of samples from 1969 and the 1979 – 1981 period are severely limited and cover a much larger segment of the river. Second, sampling methods differ in the part of the channel that was sampled, the portion of the surface/subsurface that was sampled and the sampling scheme. With this in mind, we analyzed how downstream fining changed with time. The rate at which our samples fine downstream falls roughly in the middle of the fining rates of the two historic data sets (Fig. 16). If we take the three samples from 1969 to be representative of the fining rates across the sampling domain, then it suggests that the fining rate of material downstream has lessened since this time. We suggest that a reduction in sediment supply – due to trapping by dams – provides a mechanical explanation by which the fining of material

downstream could lessen over time. Laboratory experiments that study clast abrasion in tumbling barrels show mixed results pertaining to the effect of clast 'charge', (the amount of material in the barrel) on attrition rates. Wentworth (1919) found a strong increase in attrition rates with greater clast charge; Bigelow (1984) found no effect; and Lewin and Brewer (2002) produced mixed results for different lithologies. However, there is consensus that reducing the charge reduces clast to clast effects. We hypothesize that trapping by dams (which O'Connor et al. (2014) estimates to reduce supply 67% at Albany) has had a similar effect to reduce clast to clast effects in the Willamette and its tributaries. This has led to a decrease in the rate of attrition along the mainstem Willamette, and thus the rate of fining downstream. Further, a reduction in the frequency and magnitude of flood events has likely increased the relative effect of selective-transport on downstream fining. Selective transport is dependent on stream competence (the maximum grain size a flow can entrain). Since overall stream competence has decreased in the mainstem Willamette, the preferential transport of finer grains has increased. A strong signal of selective-transport is evidenced by our observation that all gravel bars in our study segment were heavily armored. With the high variability in downstream fining between all three data sets, it appears that the processes that control fining were still equilibrating to historical disruptions to the sediment regime before 2014. However, to reiterate, any historical interpretation of grain sizes is severely limited given the constraints of the available data. More grain size measurements, with greater coverage and resolution (in time and space), would be required to draw firm conclusions.

During grain size measurements we observed that individual depositional features display high variability in grain size distribution (e.g. Fig. 26). We suggest that this reflects locally variable sediment transport dynamics that are important for the mode of bar formation. The peculiarities of multiple transport events should produce complex spatial variability of the grain texture within individual bars. Dykaar and Wigington (2000) proposed that gravel bars in the Willamette form by the sequential deposition of gravel sheets during high flow events. Modern theory and observations on similar river systems lends credence to this hypothesis. Church (2006) noted that historically dominant theory of bed load moving as a continuous carpet downstream "appears more to be an artifact of simplified models for computation than a reality of rivers". Rice et al., (2009) examined bar stratigraphy with ground-penetrating radar along the lower Fraser river and found that bars formed by the vertical accretion of gravely bedload sheets. It's important to note that the Fraser river is classified as wandering braided river which is thought to represent a transitory state between meandering rivers (such as the Willamette) and braiding rivers (Ferguson & Werritty, 1983). We observed bar morphology similar to gravel bars in the Fraser suggesting a similar mode of formation. Fig. 27 shows what appear to be sequential, overlapping gravel deposits. The two surfaces are distinguishable by a prominent leading 'toe' of the most recent deposit.

Figure 26. Location on bar 2 with high spatial diversity in surface grain sizes.

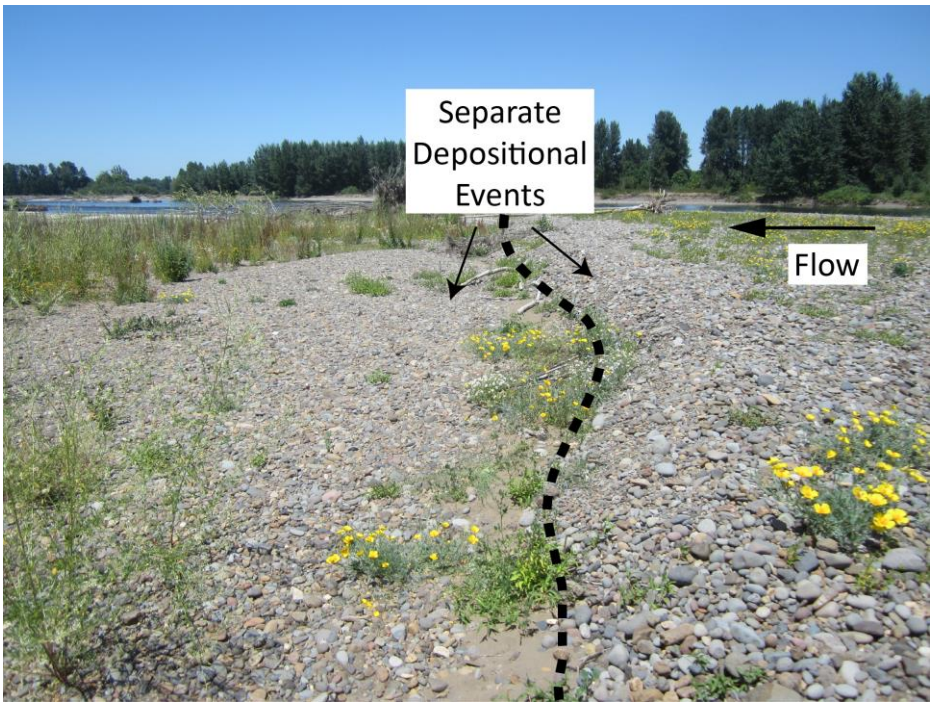

Figure 27. Distinct ‘gravel sheets’ noted by Dykaar (2000) are common on gravel bars and are likely formed by separate depositional events. Picture taken at Bar 2.

We suspect that our sampling methodology was not adequate for capturing the high level of variability in grain size distributions present in individual bar features. We believe that this led to a high-level of sampling error that masked the signal of downstream fining (and is reflected in the high p-values). The complex arrangement of deposits from multiple transport events leads to textural conditions that require fine-spatial resolution for suitable measurement. Often during sampling, the placement of a sampling transect required ad-hoc interpretation of the depositional history of the sample site. Standards of procedure also dictated that sampling transects be placed near the bar centroid. Grain sizes along the sampling transect are well represented, though bar variability outside the sampling transect is not. New methods exists that provide spatially-continuous characterization of surface grains. Photogrammetry and digital 'grain-sieving' algorithms, when taken together, can sample the two-dimensional grain size distribution of a surface. Modified sampling techniques using this method may better characterize local spatial variability of grain texture in systems such as the Upper Willamette. Capturing bar-scale variability in grain size distributions would inform the processes that drive bar evolution in the Upper Willamette River.

Structural reinforcement of the streambed via armoring is commonly exhibited by low-gradient gravel-bed rivers (Church, 2006). Qualitative assessment of surface layer armoring in the study segment suggests that the sediment supply and the river capacity to move sediment are not in equilibrium (Dietrich, Kirchner, Ikeda, & Iseya, 1989). Armoring of the surface layer is a common response of gravel-bed rivers to flow modification by dams and limits incision (Grant, 2013). As stated, dams in the

Willamette basin have reduced the competence of the river. Previously mobilized grains remain immobile while smaller grains are winnowed away.

Imbrication of the surface layer is common in rivers under transport conditions where grains move intermittently (Johansson, 1976). Imbrication of the surface layer also acts to reduce bed entrainment and incision by altering grain-scale hydraulics, effectively increasing the grain reference shear. We observed imbrication at around ¼ of the sampling locations. Better quantifying imbrication in the study segment would improve our understanding of sediment transport dynamics.

Channel Bathymetry

As stated, the shape of the synthetic channel bathymetry was not statistically significant for sediment transport. This is not surprising given the vast difference in flow conditions between the time of LiDAR capture and that of modeled floods. The LiDAR was flown during summer base-flow conditions while sediment transport was modeled for overbank flood flows. In other words, the unknown portion of the channel (the synthesized portion) was relatively small in relation to the wetted channel and overbank areas at flood stage. Further, modeling of hydraulics and sediment transport was one-dimensional. The two-dimensional nature of the bathymetry was only accounted for by scalar variables such as area and wetted perimeter. The four different channel shapes are similar by these metrics (Table 7).

As channel shape was not significant for sediment transport, the question of 'which channel shape is right?' is nullified. For this study, as in others where this is the case, other considerations should take precedent. Depending on the application,

rectangular bathymetry may be computationally simplest because width does not vary with depth (below overbank). In hindsight, it would have be useful to test the model sensitivity to cross-sections extracted directly from the LiDAR itself. It may be the case that it didn't matter whether synthetic bathymetry below the LiDAR water surface was computed or not. This information would be useful for assessing the consequences of bypassing this step altogether, to the benefit of much time saved. The problem of unknown bathymetry besets many applications of LiDAR in fluvial geomorphology. Near-infrared LiDAR is available for much of the U.S. and the question of sediment transport at flood stages is a common one. Thus it would be useful to determine the circumstances in which bathymetry below wetted LiDAR surfaces should be accounted for.

Sediment Transport Capacity

HEC-RAS was used to calculate hydraulic parameters required for sediment transport modeling. The greatest increase in hydraulic radius is seen between the 99% and 80% annual percent exceedance flows, indicating that the transition to overbank occurs around the 80% annual percent exceedance flows (1125 m^3 / s). It's important to note that we ran a 1-D model in HEC-RAS (although the latest version includes 2-D flow capabilities). 1-D modeling is not well suited for modeling flow outside the channel in the Upper Willamette. The floodplain exhibits great hydrodynamic complexity with many stage-variable connections between flood-conveying features. A fully 2-D model or a 1-D and 2-D coupled model would improve the accuracy of hydraulic calculations.

Also consider that there are multiple constrains on the validity of modeling and interpreting sediment transport rates. The transport of bed load material is highly variable in space and time (Wilcock, Pitlick, & Cui, 2009). The interaction of grains and hydraulics, and thus bed mobilization, is a stochastic process, confounding accurate prediction. As mentioned, the surface material along the reach shows a patchwork variability at local spatial scales. Hydraulic conditions, while not measured, are sure to vary greatly with hydrologic conditions and local morphology. An abundant (if not impossible) level of fine-resolution data (in space and time) is required for accurate prediction of sediment transport.

Another problem exists that is related to the equilibrium between sediment supply and demand in the Upper Willamette. Remember, the sediment transport rates we modeled in this study are understood to be the transport capacity, or the maximum rate at which transport can occur. Under equilibrium conditions the transport rate and the transport capacity are equal. However, the high level of armoring observed at all 23 bar locations indicates that transport capacity exceeds sediment supply, suggesting that model sediment transport capacity over-predicts true sediment transport rates. Disequilibrium conditions also lead to the possibility that the mobile load is quite different from the bed surface (Wilcock et al., 2009). Consequently, surface grain size measurements would be inappropriate for modeling sediment transport.

A final constraint (and perhaps the largest) is that no quantitative observations of sediment transport exist on the Upper Willamette. There is no way to gauge the accuracy of the model results against observations. Transport observations also allow for model calibration, although the Wilcock and Crowe equation does not directly incorporate

calibration information. Measuring bed load transport in the field was beyond the means of this project. Bed load sampling along a large river like the Willamette is logistically difficult and requires heavy equipment to undertake. Along the study reach there is only a single two-lane bridge (without shoulders) that crosses the river at Harrisburg. Future sampling would have to overcome these limitations.

In summary, there is great uncertainty in what is actually transported, where, when and at what rate. These issues directed the research questions. The research goal of this study was not to provide absolute predictions of sediment transport across distance and flow conditions. Rather, it was to characterize the relative distributions and patterns of potential sediment transport. There are several advantages and disadvantages to this approach. For example, many processes in natural systems are threshold limited, for instance overbank flow. Relative or probabilistic description cannot account for threshold values. However, there is utility in dimensionless analysis. Consider that a ratio of two predictions holds even when the two predictions are off by some factor. Hence, pattern can be preserved in the face of gross scaling errors; in other words, pattern is scale-independent. This is less-so the case with sediment transport since the governing relationships are highly non-linear, but the general theory is still applicable. The spatial distribution of sediment transport rates is more accurate than the magnitude of those rates.

Results suggest that sediment transport is discrete with longitudinal distance whereby peaks are seen to punctuate reaches of relatively even transport rates (Fig. 21) The distribution of transport rates is generally consistent across the range of flows modeled. Locations that display high rates of sediment transport tend to increase non-

linearly with discharge (particularly above the 20% annual exceedance). The portion of the reach upstream of river kilometer 20 has relatively few peaks in the sediment transport rate and overall low sediment transport rates. The same is true between 31 and 41 km and downstream of 56 km, suggesting that significant continuous expanses of the Upper Willamette have relatively minor capacity to move sediment compared to the reach maximum.

Two locations have significantly higher transport rates than all others. One is located at river kilometer 21 and the other at river kilometer 53. Fig. 28 shows the floodplain topography and longitudinal pattern of flow normalized sediment transport rate at each location. There are several morphological characteristics that these two sites have in common. Both show strong disconnection from the floodplain. Floodplain surfaces on the left bank consist of high surfaces of swales with little side-channels or paleo-channels. Both abut a high terrace on the right bank stabilized by resistant Pleistocene gravels or revetments (not shown). Upstream of these locations there is a relatively greater number of secondary features that may act to convey flow during overbank conditions. During high stage, flood waters becomes confined to the main channel as they enter these sections of the river. Disconnection from the floodplain and high sediment capacity are self-replicating process. High transport capacity leads to incision and disconnection from the floodplain which in turn concentrates flow in the main channel and increases transport capacity.

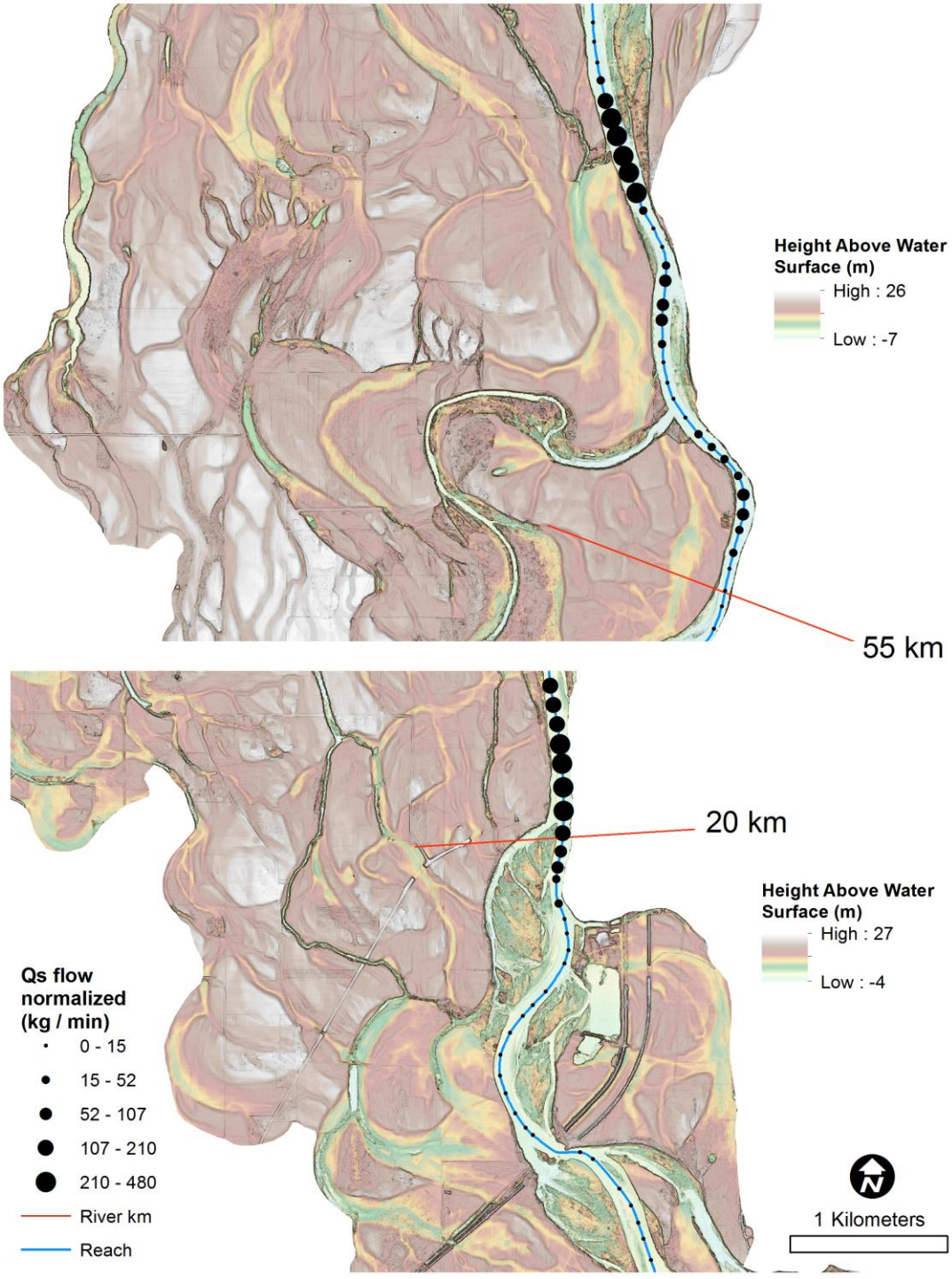

Figure 28. Flow normalized sediment transport rate at study segment locations with the two highest magnitudes.

Klingeman's work in the 1970's found that incipient motion occurs only several times a year during peak flow. Coupled with the spatial results of this study, the findings suggest a sediment transport regime that is dominated by mobilization at a very small subset of space and time positions. What would this mean for loading processes? Spatially *continuous* sediment loading should necessarily result in morphologically gradational depositional surfaces. Spatially *discontinuous* sediment loading should conversely result in morphologically discretized depositional surfaces. Observations of gravel surface morphology points to a patchwork of depositional events, commensurate with the later. Individual pulses of sediment may provide an explanation for observations of bar morphology, in which each pulse corresponds to a distinctive 'sheet' (Dykaar & Wigington, 2000) (Fig. 27).

Change in Bare Gravel Surfaces

The distribution of gravel is controlled by both fluvial and vegetative processes. Gravel may be removed from the system by downstream transport out of the segment, lateral deposition in storage features or vegetation encroaching onto gravel surfaces (Wallick et al., 2013). Gravel is introduced to the system from tributaries, bank erosion, scouring of vegetated features and by exposure of new landforms by avulsions. Large floods are critical for introducing gravel into the Willamette and resetting vegetative succession patterns (Dykaar & Wigington, 2000; Klingeman, 1987; Wallick et al., 2013). Aerial mapping of bare gravel surfaces is difficult to tie to process since multiple processes can produce the same result. For example, loss of bare gravel in a bar feature

may be due to either vegetative encroachment or scouring and excavation of gravel. Both vegetative and transport processes are occurring on the Willamette and their relative contribution to change in bare gravel surfaces is not well quantified in this study. Further, our analyses are limited by the temporal spacing of our data since the processes that control gravel bar distribution act on time scales less than one year (the smallest temporal increment) as well as on time scales greater than the mapping period.

Reach-scale change in gravel bar area for the years 2005 through 2009 appears to tell the story of gravel influx into the system and subsequent removal out of the system. The 2006 WY winter peak flow (a ~7 year return event) introduced 24% more bare gravel in the study segment. The relative contribution of gravel from upstream and lateral storage is difficult to quantify. Avulsions during the 2006 flood season (Fig. 29) indicate that a significant portion of sediment was sourced from lateral storage and scouring of floodplain surfaces. This is also consistent with finding of Klingeman (1987) that bank erosion may be the primary source of gravel replenishment in most years. The period between 2006 WY and 2009 WY shows a subsequent 53% loss in gravel surfaces, larger than that gained between water years 2005 WY and 2006 WY. Examination of the imagery leads us to conclude that most active gravel was lost via vegetative encroachment rather than downstream flushing or lateral deposition. Fig. 29 shows vegetation encroaching onto bare gravel surfaces at Buckskin Mary's Landing between water years 2006 WY and 2009 WY. The peak flow between 2007 WY and 2011 WY was 1671 m^3/s (a ~2 year return event) occurring in the winter of 2009, before the corresponding imagery flown that year. The influx of gravel in 2006 WY and subsequent

removal suggests that minimum flows required to replenish active gravel in the system are greater than 1671 m^3/s and less than 2073 m^3/s at Harrisburg.

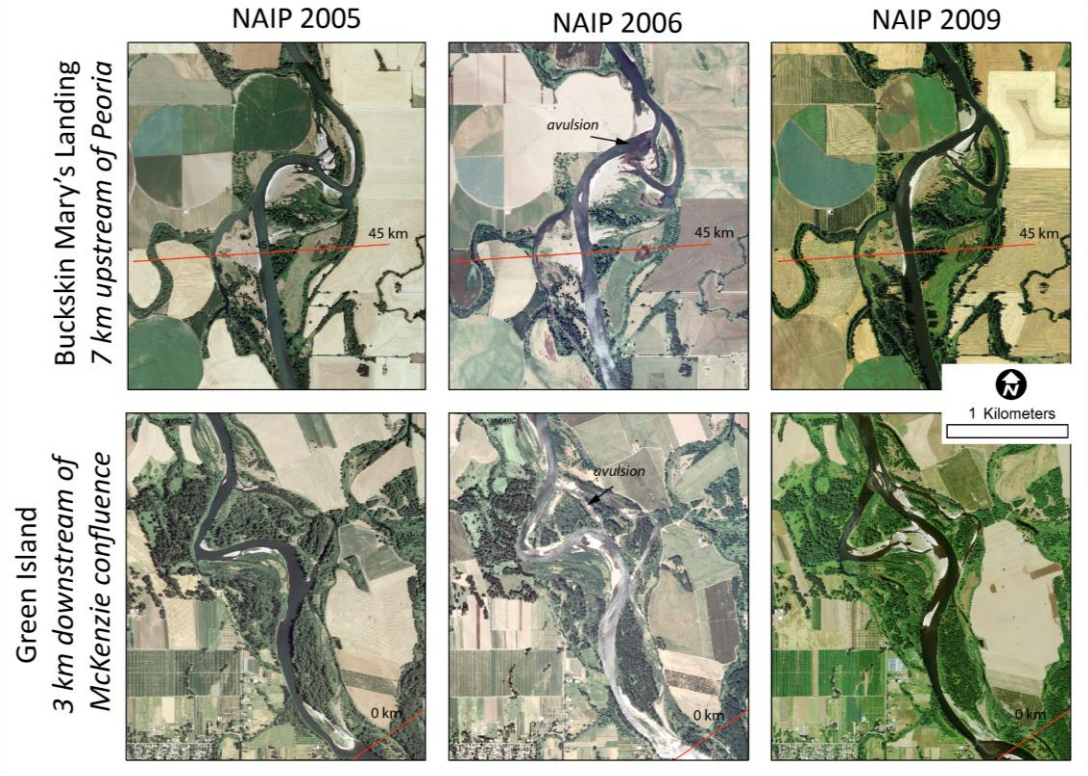

Figure 29. Geomorphic change during the mapping period at two dynamic areas of the study segment.

Consider the observation that many reaches consistently have no gravel present. Surely, sediment has traversed through these points during the mapping period. It must then be the case that all sediment entering these reaches is fully evacuated, if vertical adjustment in the channel bed is ruled out (a specific gage analysis using the USGS streamflow gage at Harrisburg by Wallick et al. (2013) found that the vertical position of the channel was relatively stable during the mapping period). Moreover, O'Connor et al. (2014) found that bar-area can be used to predict bed-material supply for alluvial rivers in western Oregon. We assert that net transport capacity exceeds net sediment supply for all

flow and sediment conditions during transportation events where little or no gravel is seen to occur in the study segment. These locations could aid in estimating upper bounds on sediment supply in the Upper Willamette. This would entail constructing accurate bed load rating curves for reaches where there is consistently little to no active gravel.

The strong alignment between the distribution of transport rates and active gravel suggests that sediment transport rates are sufficient for predicting the absence (and presence) of depositional surfaces in longitudinal space. Further, the data seem to reflect a transport regime that frequently alternates between supply limited and capacity limited conditions. Supply limited conditions are often associated with lesser gravel bars and lower lateral migration rates, while the converse is true for capacity limited conditions (Church, 2006; O'Connor et al., 2014).

Supply limited segments are those highlighted in gray in Fig. 25 where the transport rate is high and the amount of gravel is low. All other reaches are capacity limited or in equilibrium by negation. The spatial frequency at which this alternation occurs is highest downstream of Harrisburg (river kilometer 20). By comparison, the balance between supply and capacity in the river upstream of this point alternates at a much lower spatial frequency. Upstream of Harrisburg the active channel includes many secondary features, flows through poorly consolidated Holocene alluvium and has a relatively low meander rate (Fig. 2, Fig. 22). At no point does the river run up against high terraces that flank the geomorphic floodplain. Downstream of Harrisburg, the active channel is narrower and more disconnected from the floodplain. The meander frequency increases and the channel more often runs up against high terrace banks immobilized by poorly-cemented Pleistocene gravels (Fig. 2, Fig. 22). Zones of high sediment transport

often coincide with areas of high curvature. Fluid forces become concentrated in areas of high river curvature, shear velocities increase as well as sediment capacity. Our hydraulic calculations were done in HEC-RAS as a one-dimensional model. Planform is accounted for by distributing the center of mass of channel and overbank flow along the channel flow path and overbank flow paths respectively. Our results suggest that 1-D hydraulic modeling in HEC-RAS coupled with 1-D sediment transport modeling does moderately-well to capture sediment transport dynamics associated with planform.

It is important to note that we did not consider the distribution of bank revetments in this analysis. Bank revetments have a very low erodibility (Wallick et al. (2006) estimate 0.015 ± 0.028) and exert large control on lateral and vertical adjustments of the channel (Wallick et al., 2013) as well as sediment supply in the Willamette River (Klingeman, 1987). Recent mapping has found that roughly 45% of banks between Eugene and Harrisburg and 26% of banks between Eugene and Portland are protected by revetments (Stanley Gregory, 2007; Wallick et al., 2006). In our modeling approach, bank material is not a parameter because the model is not dynamic, i.e. there is no vertical or lateral adjustment of the channel. Since the model does well at predicting low-gravel patches in the study segment, we conclude that bank revetments are not directly linked to the distribution of low-gravel patches. Consider that revetments are often used to stabilize banks with high lateral mobility. Little gravel is expected in these reaches because high lateral mobility is associated with high stream capacity. An argument can be made that reach-scale transport dynamics should have adjusted to revetments and thus their distribution should affect the pattern of supply and capacity limited conditions. However we argue that large-scale morphologic features of the floodplain and channel

drive the hydraulics of large floods that control the distribution of gravel within the study segment. Further, the position of revetments does not appear to strongly affect these large-scale morphological features (or the effect has not yet been actualized).

In summary, we argue that reach-scale morphological features related to river planform and the position of the channel relative to geologic units controls the spatial frequency of peaks in sediment capacity. Connection to the floodplain and the morphology of secondary features that convey flow during flood events explain the relative magnitude of peaks in the sediment capacity. Additional insight would be gained by examining the relationships between channel confinement, meander frequency, the longitudinal pattern of active gravel and sediment transport rates.

Lastly, we consider the impact of sediment trapping by dams on the distribution of active gravel surfaces. Several assumptions need to be made. Looking back at Fig. 25, we identified the smallest spike in the flow normalized sediment transport rate that corresponded to an absence of gravel during the mapping period. We take this to be a threshold value in sediment capacity to predict reaches with no or little gravel. Essentially we consider sediment supply and transport capacity to be in equilibrium at this point. Since supply and capacity are equal, supply is known and we can adjust this number by the percentage trapped behind dams (the units are meaningless because we conflate transport capacity with yield). Fig. 30 shows the effect of increasing this threshold value by 67%, as estimated by O'Connor et al. (2014) (this number is calculated below the confluence with the Santiam - about 40 km downstream of our study segment).

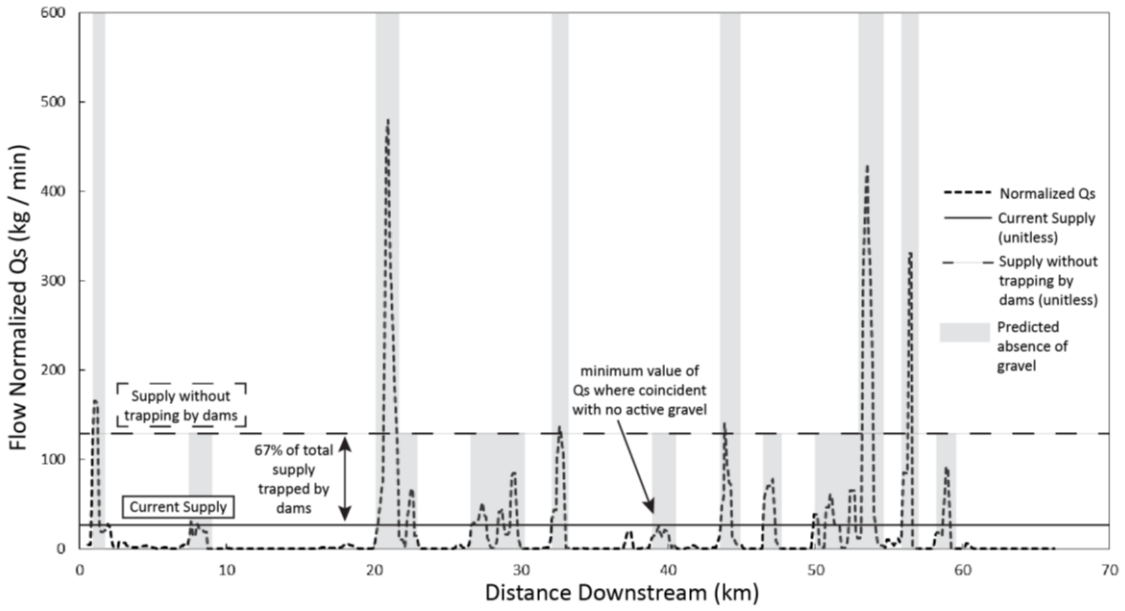

Figure 30. A simplified approach to test the effect of sediment trapping by dams on the distribution of active gravel in the Upper Willamette. Absence of gravel is predicted where the flow normalized sediment transport rates is above the corresponding line indicating supply with or without trapping by dams.

This simplified approach suggests that trapping by dams has greatly decreased the total longitudinal length of active gravel and modified its distribution. With trapping, there are over twice as many segments where no active gravel is found compared to what we predict would be the case without trapping. Further, segments between areas with no active gravel are much shorter on average. The distribution of gravel has direct implications for aquatic stream ecology since gravel is key for habitat formation. For example, Hulse et al., (2007) found that cold water refugia in the Upper Willamette, created by hyporheic flow through gravel features, allow salmonids to traverse segments of the river that exceed there thermal tolerance. The importance of gravel features for cold water refugia is likely to increase during the 21st century as water temperature in the Willamette is predicted to increase during the summer months (Jaeger, Plantinga, Haggerty, & Langpap, 2014).

CHAPTER VI

CONCLUSION

In the introductory section, we posed the following research question: *what are the key characteristics of the modern sediment transport regime, and what is the longitudinal pattern of these characteristics in the Upper Willamette River, Oregon?* We conclude by summarizing the characteristics that we find to be most definitive of modern sediment transport dynamics.

All bars are heavily armored and ¼ have some degree of structural imbrication. Armoring is indicative of supply-limited conditions and suggests that selective sorting drives spatial variability in grain sizes. Grain size fines gently downstream (the D_{16} size fraction was found to be most significant at a rate of 0.11 mm per river km). We suggest that selective sorting dominates fining rates downstream. We also believe that the signal of grain fining is partly masked by grain variability at the bar scale and that our sampling methods were inadequate in capturing variability at this scale. The rate of downstream fining falls between the rates of downstream fining of data collected in 1969 and between 1979 and 1981. The data are largely inclusive but may suggest there has been a decrease in the downstream fining rate since 1969. We hypothesize that a reduction in the sediment supply due to trapping by dams has reduced clast to clast interaction and thus has reduced the rate of attrition in the mainstem as well. We found that the unit stream power of large flows does not correlate with grain size, suggesting that no one single flow conditions dominates in shaping bar surfaces.

Sediment transport rates are highly discrete with longitudinally distance, exhibit similar longitudinal patterns across flows and increase non-linearly with flow. The

highest sediment transport rates are found where the channel is confined due to disconnection with the floodplain and is bounded on one side by resistant terraces.

Bare gravel bar area was mapped from NAIP imagery for water years 2005, 2006, 2009 and 2011. A large influx of gravel was seen following flows in the winter of 2006. Following this, active gravel bar area diminished primarily by re-vegetation. The data suggest that flows greater than at least 1671 m^3/s (a ~2 year return event) and less than 2073 m^3/s (a ~5 year event) at Harrisburg are required to reintroduce active gravel into the system and reactivate temporarily stabilized bars.

Peaks in the sediment transport rates coincide with areas of low active gravel. There were few locations in which this relationship did not hold. The spatial distribution of supply limited conditions and active gravel surfaces are tightly linked. Downstream of Harrisburg (river kilometer 20), peaks in sediment transport rates are more frequent and higher in magnitude. The distribution of active gravel also shows more frequent oscillation between high and low values. We believe that meander frequency, connectivity with the floodplain and the channel position in relation to geologic units is responsible for the observed longitudinal pattern of active gravel and sediment transport rates. Finally, we conclude that trapping by dams has increased the length and concentration of 'no gravel' patches to the detriment of stream ecology.

There are several methodological findings of importance. We found that the choice of synthetic channel bathymetry shape was not significant for sediment transport rates at high flows. This is intuitive given the relatively low unknown portion of the channel and the one-dimensional aspect of modeling. We also believe that 2-D hydraulic modeling is necessary for capturing complex hydrodynamics of overbank surfaces in

dynamic alluvial systems such as the Upper Willamette River. Further, we suggest that grain size sampling methods be included in subsequent studies that capture variability of the grains within individual bar features. This would aid in defining clast fining downstream and contribute to our understanding of bar formation and evolution.

Our findings in this study lend key insights into the sediment transport regime of the Upper Willamette River. The importance of sediment transport for society is vast with consequences for species habitat, floodplain hydrology, vegetation succession, river dynamism and much more. Within our study segment, the distribution and diversity of aquatic habitats are at the forefront of restoration concerns. Our results inform these interests by linking the distribution of gravel to sediment transport rates. Further we have discussed the mode of bar formation and sought to tie sediment dynamics to floodplain morphology.

Sediment dynamics of the Upper Willamette have long been considered but little studied. Here we strive to lay an additional foundational stone in our understanding of the Upper Willamette's sediment transport regime. The results of this study are limited by the one-dimensional modeling approach, restricted inter-bar and sub-surface grain size sampling, and the lack of bed load transport observations. Further, we did not consider the position of bank revetments which are known to be critical for channel morphodynamics (Wallick et al., 2013). Additional empirical work is needed to constrain absolute values of sediment transport and construct a balanced, reach-scale sediment budget for the Upper Willamette River. A sediment budget would be of unequaled benefit for all future geomorphic studies.

APPENDIX A

CHARACTERISTIC GRAIN SIZE VALUES AT SAMPLE LOCATIONS

Bar ID	Distance Downstream	D_{16}	D_{50}	D_{84}
-	km	mm	mm	mm
1	3.1	13.3	24.0	37.8
2	3.6	20.8	37.0	59.3
3	4.3	24.4	43.6	76.9
4	5.7	14.8	30.3	68.1
5	6.2	27.5	43.4	69.9
6	13.7	25.1	46.3	84.9
7	15.8	22.4	35.9	59.6
8	18.5	14.7	27.7	45.0
9	19.0	21.1	36.2	56.4
10	20.9	23.0	33.3	55.3
11	22.3	16.0	26.0	41.9
12	23.8	17.3	26.6	41.0
13	25.4	26.0	44.7	69.0
14	30.1	11.6	20.6	34.7
15	33.8	12.7	20.4	33.1
16	35.8	19.4	30.1	44.7
17	37.4	12.6	20.3	33.1
18	40.9	13.5	31.6	57.1
19	43.4	16.7	35.9	62.5
20	45.6	19.5	33.9	53.7
21	48.1	12.9	32.6	57.5
22	49.8	18.3	28.8	42.7
23	57.2	17.5	34.1	54.2

APPENDIX B

PHOTOGRAPHS OF GRAIN SAMPLING LOCATIONS

Bar 1 ‘Green Island’

Bar 2 ‘Power Line Bar’

Bar 3 ‘Lone Pine Drive’

Bar 4 ‘Maple Drive’

Bar 5 ‘Lanes Turn Rd’

Bar 6 ‘Blue Ruin Island’

Bar 7 ‘Downstream of Harper’s Bend’

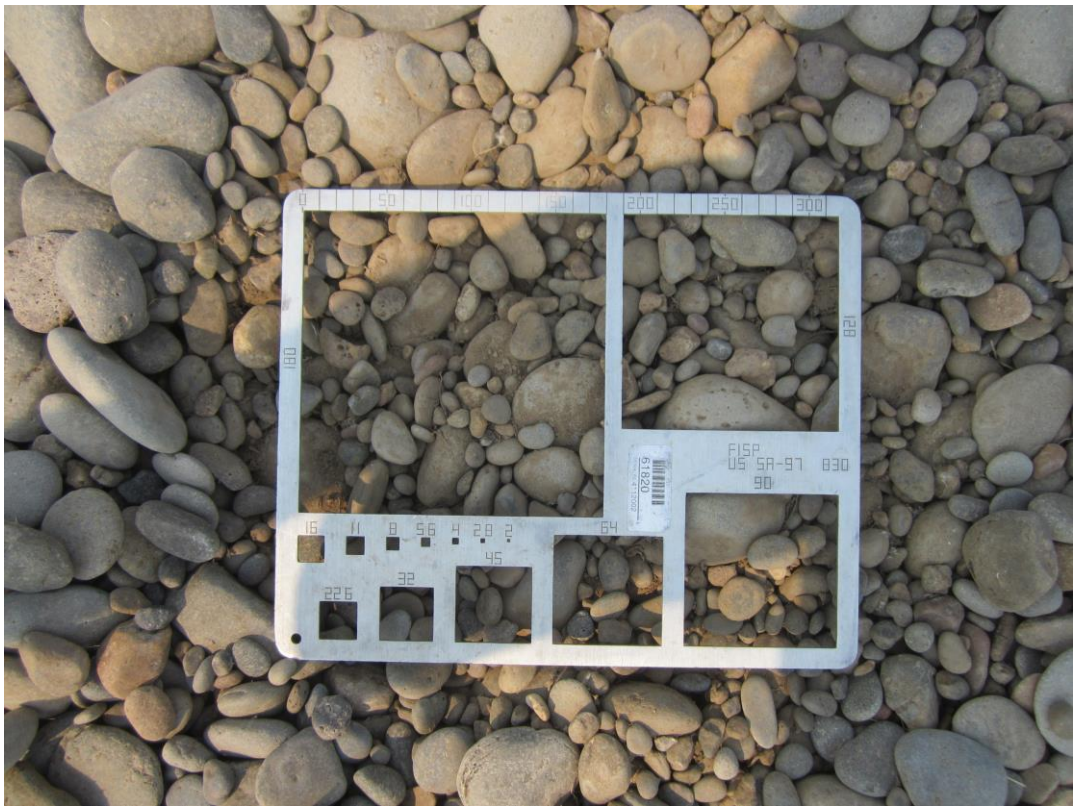

Bar 8 ‘Downstream of Curtis Slough’

Bar 9 ‘Upstream of Harrisburg’

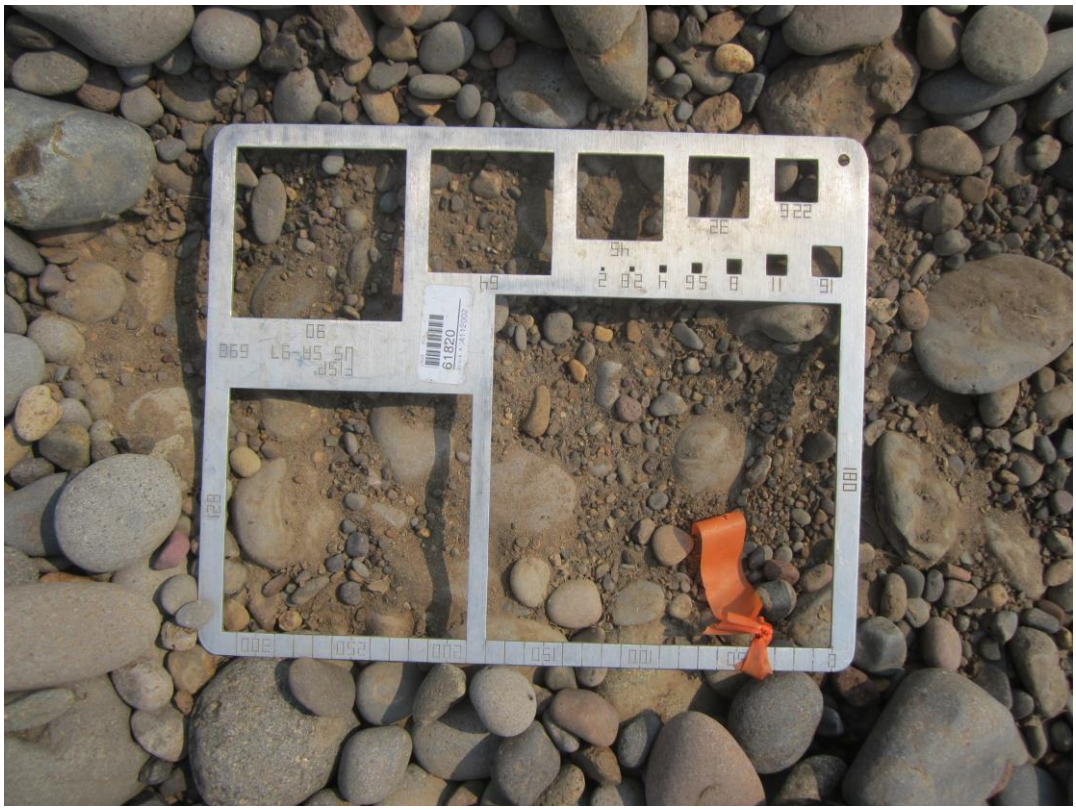

Bar 10 ‘Harrisburg Landing’

Bar 11 ‘River Life Resort’

Bar 15 ‘Anderson County Park’

Bar 16 ‘Upstream of Irish Bend’

Bar 17 ‘Irish Bend’

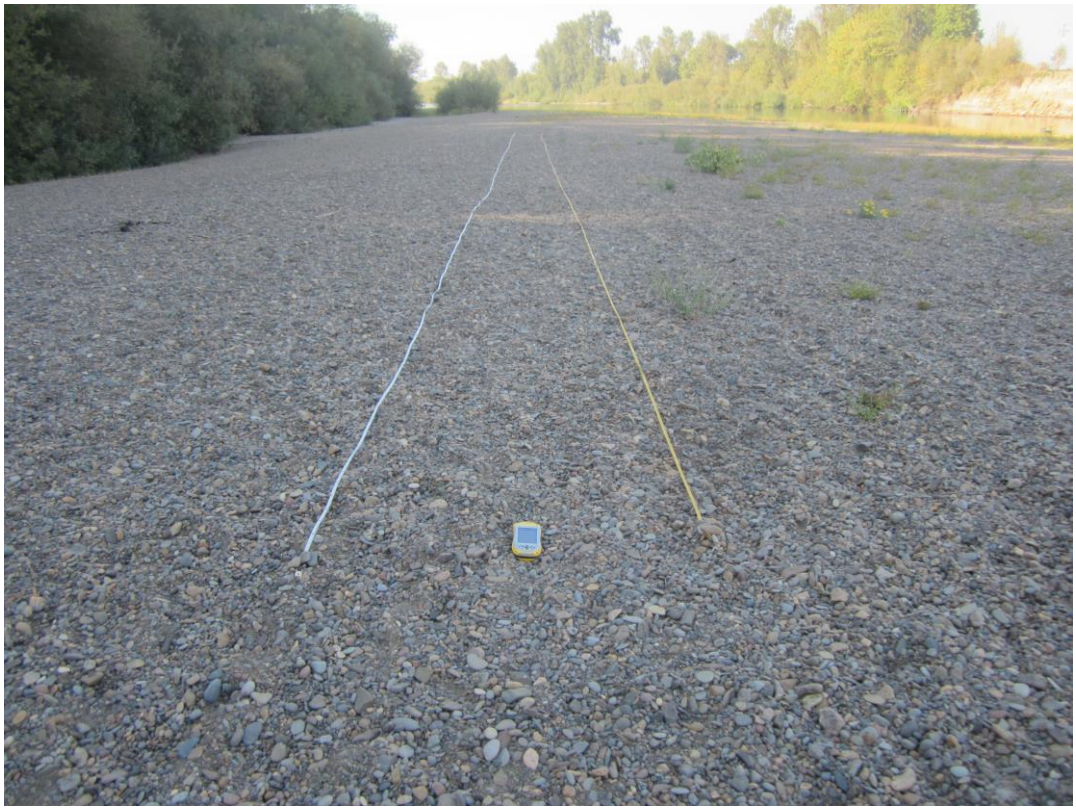

Bar 18 ‘Norwood Island’

Bar 19 ‘Eureka Road’

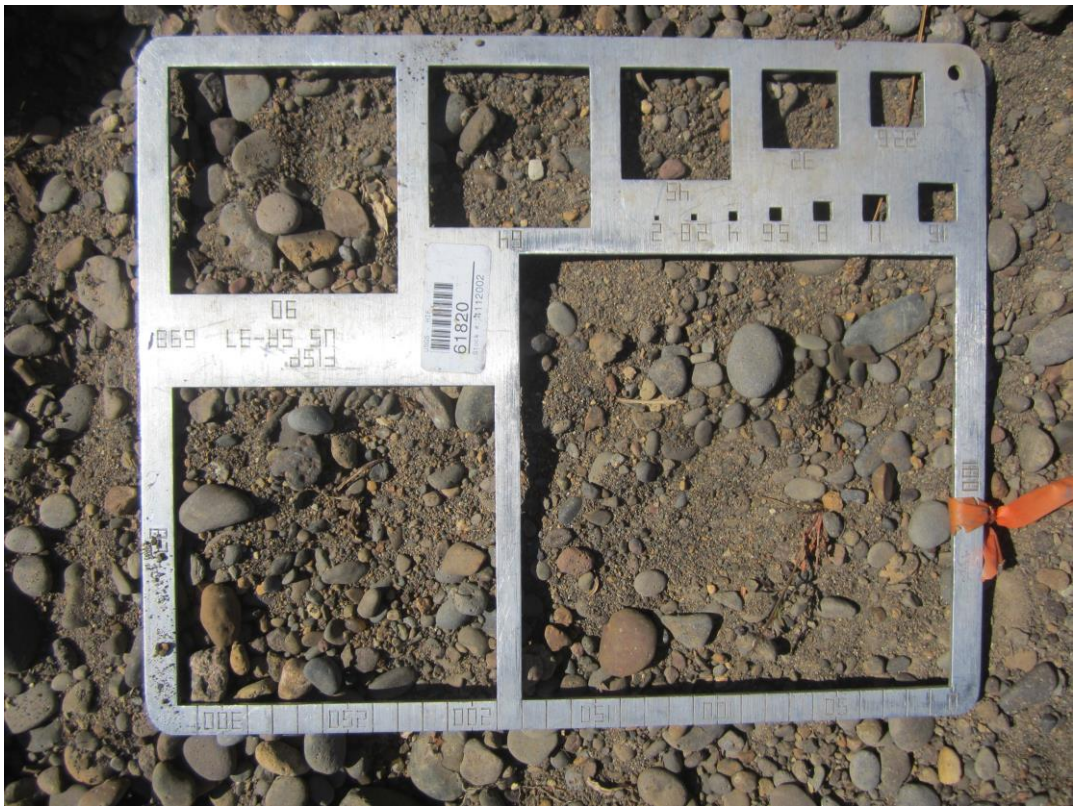

Bar 20 ‘Buckskin Mary’s Landing’

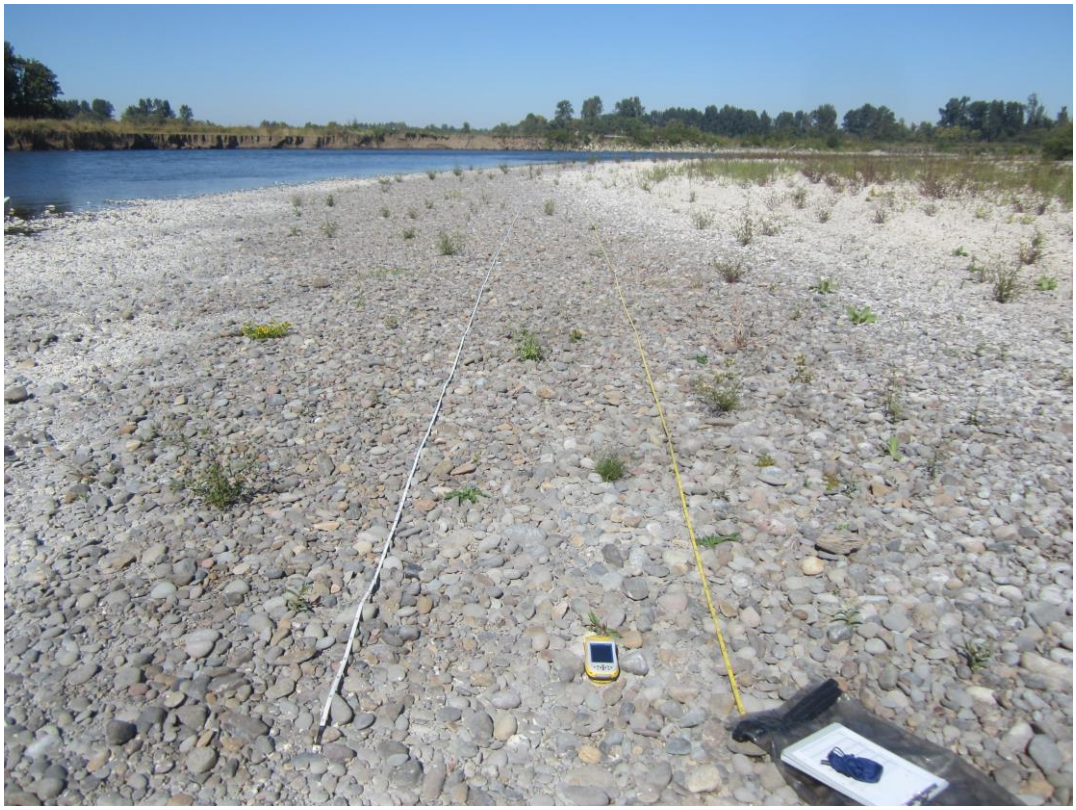

Bar 21 ‘Snag Boat Bend’

Bar 22 ‘Oxbow Orchard’

REFERENCES CITED

About our Willamette Valley locations. (2015). Retrieved 5/19/2015, from http://www.nwp.usace.army.mil/Locations/WillametteValley.aspx

Annual Reports of Chief of Engineers for the year 1875, Part II. (1875). Washington, DC.: U.S. Army Corps of Engineers.

Baker, J. P., Hulse, D. W., Gregory, S. V., White, D., Van Sickle, J., Berger, P. A., . . . Schumaker, N. H. (2004). Alternative futures for the Willamette River basin, Oregon. *Ecological Applications, 14*(2), 313-324.

Benner, P. A., & Sedell, J. R. (1997). Upper Willamette River landscape: a historic perspective. In A. Laenen & D. A. Dunette (Eds.), *River quality: dynamics and restoration* (pp. 23-47). Salem, Massachusetts: CRC Press.

Bigelow, G. E. (1984). Simulation of pebble abrasion on coastal benches by transgressive waves. *Earth Surface Processes and Landforms, 9*(4), 383-390. doi: 10.1002/esp.3290090411

Bruner, G. (2010). HEC-RAS River Analysis System: Hydraulic Reference Manual. Davis, CA: USACE Hydrologic Engineering Center.

Church, M. (1978). Attrition (abrasion), fluvial *Encyclopedia of Earth Science* (pp. 40-42): Springer Berlin Heidelberg.

Church, M. (2006). Bed material transport and the morphology of alluvial river channels. *Annu. Rev. Earth Planet. Sci., 34*, 325-354.

Conyers, M. M., & Fonstad, M. A. (2005). The unusual channel resistance of the Texas Hill Country and its effect on flood flow predictions. *Physical Geography, 26*(5), 379-395.

Dietrich, W. E., Kirchner, J. W., Ikeda, H., & Iseya, F. (1989). Sediment supply and the development of the coarse surface layer in gravel-bedded rivers. *Nature, 340*(6230), 215-217.

Dykaar, B. B., & Wigington, J., PJ. (2000). Floodplain formation and cottonwood colonization patterns on the Willamette River, Oregon, USA. *Environmental Management, 25*(1), 87-104.

Ferguson, R., & Werritty, A. (1983). Bar development and channel changes in the gravelly River Feshie, Scotland. *Modern and ancient fluvial systems*, 181-193.

Fierke, M. K., & Kauffman, J. B. (2006). Riverscape-level patterns of riparian plant diversity along a successional gradient, Willamette River, Oregon. *Plant Ecology, 185*(1), 85-95.

Fonstad, M. A., & Marcus, W. A. (2005). Remote sensing of stream depths with hydraulically assisted bathymetry (HAB) models. *Geomorphology, 72*(1), 320-339.

Grant, G. E. (2012). The geomorphic response of gravel-bed rivers to dams: perspectives and prospects. *Gravel-Bed Rivers: Processes, Tools, Environments*, 165-181.

Gregory, S. (2007). Historical channel modification and floodplain forest decline: implications for conservation and restoration of a large floodplain river – Willamette River, Oregon. In H. P. Helmut Habersack & R. Massimo (Eds.), *Developments in Earth Surface Processes* (Vol. Volume 11, pp. 763-777): Elsevier.

Gregory, S., Ashkenas, L., Oetter, D., Minear, P., & Wildman, K. (2002). Historical Willamette River channel change. *Willamette River Basin Planning Atlas: Trajectories of Environmental and Ecological Change. Oregon State University Press, Corvallis, Oregon*, 18-26.

Gregory, S. V., Ashkenas, L., & Nygaard, C. (2007). Summary report to assist development of ecosystem flow recommendations for the Coast Fork and Middle Fork of the Willamette River, Oregon: Institute for Water and Watersheds, Oregon State University.

Gregory, S. V., & Bisson, P. A. (1997). Degradation and loss of anadromous salmonid habitat in the Pacific Northwest *Pacific Salmon & Their Ecosystems* (pp. 277-314): Springer.

Guidelines for Determining Flood Flow Frequency. (1981): Interagency Advisory Committee on Water Data. USGS Bulletin #17B of the Hydrology Subcommittee. (pp. 194).

Hulse, D., Gregory, S., & Baker, J. (2002). *Willamette River Basin Planning Atlas*. Corvallis, OR: Oregon State University Press.

Hulse, D. W., Branscomb, A., Enright, C., Gregory, S. V., & Wildman, R. (2007). Linking cold-water refuges into a biologically effective network in the southern Willamette River floodplain: outlining key locations and knowledge gaps. *Mid-Willamette Valley Council of Governments, Portland, Oregon*.

Jacobson, R. B., O'Connor, J. E., & Oguchi, T. (2003). Surficial geologic tools in fluvial geomorphology *Tools in fluvial geomorphology* (pp. 23-57): John Wiley & Sons, Ltd.

Jaeger, W., Plantinga, A., Haggerty, R., & Langpap, C. (2014). Anticipating Water Scarcity with Climate Change in the US Pacific Northwest Using a Landscape Model of a Coupled Natural-Human System.

Johannessen, C. L., Davenport, W. A., Millet, A., & McWilliams, S. (1971). The Vegetation of the Willamette Valley. *Annals of the Association of American Geographers, 61*(2), 286-302.

Johansson, C. E. (1976). Structural Studies of Frictional Sediments. *Geografiska Annaler. Series A, Physical Geography, 58*(4), 201-301. doi: 10.2307/520535

Klingeman, P. (1973). Indications of streambed degradation in the Willamette Valley: Corvallis, Oregon, Oregon State University. *Water Resources Research Institute Report WRRI-21*.

Klingeman, P. (1987). Geomorphic influences on sediment transport in the Willamette River. *IAHS-AISH*
publication (165), 365-374.

Kondolf, G. M., Lisle, T. E., & Wolman, G. M. (2003). Bed sediment measurement *Tools in fluvial geomorphology* (pp. 347-395): John Wiley & Sons, Ltd.

Lane, S. N., & Richards, K. S. (1997). Linking river channel form and process: time, space and causality revisited. *Earth Surface Processes and Landforms, 22*(3), 249-260.

Lewin, J., & Brewer, P. A. (2002). Laboratory simulation of clast abrasion. *Earth Surface Processes and Landforms, 27*(2), 145-164. doi: 10.1002/esp.306

Madin, I. (2015). *2009 Oregon Department of Geology and Mineral Industries (DOGAMI) Oregon Lidar: Willamette Valley*.

Miller, K. L., Szabó, T., Jerolmack, D. J., & Domokos, G. (2014). Quantifying the significance of abrasion and selective transport for downstream fluvial grain size evolution. *Journal of Geophysical Research: Earth Surface, 119*(11), 2412-2429. doi: 10.1002/2014JF003156

O'Connor, J. E., Mangano, J. F., Anderson, S. W., Wallick, J. R., Jones, K. L., & Keith, M. K. (2014). Geologic and physiographic controls on bed-material yield, transport, and channel morphology for alluvial and bedrock rivers, western Oregon. *Geological Society of America Bulletin, 126*(2014), 337-397. doi: 10.1130/b30831.1

O'Connor, J. E., Sarna-Wojcick, A., Woznikak, K. C., Polette, D. J., & Fleck, R. J. (2001). Origin, extent, and thickness of Quaternary geologic units in the Willamette Valley, Oregon (pp. 51): U.S. Geological Survey.

Reid, L. M., & Dunne, T. (2005). Sediment Budgets as an Organizing Framework in Fluvial Geomorphology *Tools in Fluvial Geomorphology* (pp. 463-500): John Wiley & Sons, Ltd.

Reports of the Secretary of War. Reports of the Chief of Engineers, 1875-1899. *House executive documents, sessions of Congress*. Washington, D.C.

Rice, S., & Church, M. (1998). Grain size along two gravel-bed rivers: statistical variation, spatial pattern and sedimentary links. *Earth Surface Processes and Landforms, 23*(4), 345-363.

Rice, S., Stoffel, M., Turowski, J. M., & Wolf, A. (2012). Disturbance regimes at the interface of geomorphology and ecology. *Earth Surface Processes and Landforms, 37*(15), 1678-1682.

Rice, S. P., Church, M., Wooldridge, C. L., & Hickin, E. J. (2009). Morphology and evolution of bars in a wandering gravel-bed river; lower Fraser river, British Columbia, Canada. *Sedimentology, 56*(3), 709-736.

Risley, J., Wallick, J. R., Waite, I., & Stonewall, A. (2010). Development of an environmental flow framework for the McKenzie River basin, Oregon: U.S. Department of the Interior, U.S. Geological Survey.

Rounds, S. (2003). USGS bathymetric survey of the main stem Willamette River. Portland, OR: U.S. Geological Survey.

Sedell, J. R., & Froggatt, J. L. (1984). Importance of streamside forests to large rivers: the isolation of the Willamette River, Oregon, USA, from its floodplain by snagging and streamside forest removal. *Verh. Internat. Verein. Limnol, 22*, 1828-1834.

Sternberg, H. (1875). Untersuchungen über längen- und querprofil geschiebeführender Flüsse. *Zeitschrift für Bauwesen, 25.*

USGS. Peak streamflow for Willamette River at Harrisburg. Retrieved October 20, 2014, 2014, from http://nwis.waterdata.usgs.gov/usa/nwis/peak/?site_no=14166000

Wallick, J. R., Grant, G. E., Lancaster, S. T., Bolte, J. P., & Denlinger, R. P. (2007). Patterns and controls on historical channel change in the Willamette River, Oregon, USA. In A. Gupta (Ed.), Large rivers: geomorphology and management (pp. 491-516). Chichester, UK: John Wiley & Sons Ltd.

Wallick, J. R., Jones, K. L., O'Connor, J. E., Keith, M. K., Hulse, D., & Gregory, S. V. (2013). Geomorphic and Vegetation Processes of the Willamette River Floodplain, Oregon—Current Understanding and Unanswered Questions (pp. 70).

Wallick, J. R., Lancaster, S. T., & Bolte, J. P. (2006). Determination of bank erodibility for natural and anthropogenic bank materials using a model of lateral migration and observed erosion along the Willamette River, Oregon, USA. River Research and Applications, 22(6), 631-649.

Wentworth, C. K. (1919). A Laboratory and Field Study of Cobble Abrasion. The Journal of Geology, 27(7), 507-521. doi: 10.2307/30058414

Wilcock, P. R., & Crowe, J. C. (2003). Surface-based transport model for mixed-size sediment. Journal of Hydraulic Engineering, 129(2), 120-128.

Wilcock, P. R., Pitlick, J., & Cui, Y. (2009). Sediment transport primer: estimating bed-material transport in gravel-bed rivers (pp. 78). Fort Collins, Colorado: U.S. Department of Agriculture, Forest Service, Rocky Mountain Research Station.